SAM Code Enhancement, Validation, and Reference Model Development for Fluoride-salt-cooled High-temperature Reactors

Nuclear Science and Engineering Division

SAM Code Enhancement, Validation, and Reference Model Development for Fluoride-salt-cooled High-temperature Reactors

prepared by
Daniel O'Grady, Travis Mui, Alvin Lee, Ling Zou, Guojun Hu, Rui Hu
Nuclear Science and Engineering Division, Argonne National Laboratory

ABSTRACT

The System Analysis Module (SAM) is under development at Argonne National Laboratory as a modern system-level modeling and simulation tool for advanced non-light water reactor safety analyses. It utilizes the object-oriented application framework MOOSE to leverage the modern software environment and advanced numerical methods. The capabilities of SAM are being extended to enable the transient modeling, analysis, and design of various advanced nuclear reactor systems. This report summarizes recent progress under DOE-NE's Nuclear Energy Advanced Modeling and Simulation program in SAM code development, demonstration, and validation to support transient safety analysis of Fluoride-salt-cooled High-temperature Reactors.

The 1-D spherical geometry heat conduction model is implemented in SAM and verified with several verification test cases. The porous medium pressure drop correlations for pebble bed are converted and implemented into the 1-D fluid flow model to support the modeling of 1-D system models with pebble beds. A reference primary loop model of PB-FHR is developed, based on the UC Berkeley Mk1 FHR design and incorporated some design features in Kairos Power's KP-FHR core. A reference standard problem of the reactor primary loop model is foundational to the methodologies employed by NRC to verify the adequacy of computer codes and evaluation models. Additional SAM validation is successfully performed against CIET LOFC experiments. Good agreements between the SAM simulation results and the experimental data are obtained during the entire LOFC transient.

Table of Contents

LIST OF FIGURES

LIST OF TABLES

1 Introduction

An advanced system analysis tool, SAM [1, 2] is under development at Argonne National Laboratory for advanced non-LWR reactor safety analysis. It aims to provide fast-running, modest-fidelity, whole-plant transient analyses capabilities, which are essential for fast turnaround design scoping and engineering analyses of advanced reactor concepts. While SAM is being developed as a system-level modeling and simulation tool, advanced modeling techniques being implemented include a reduced-order three-dimensional module [3], pseudo 3-D conjugate heat transfer modeling in reactor core [4], flexible and multi-scale modeling of heat transfer between fluid and structures [5], in addition to the advances in software environments and design, and numerical methods.

SAM aims to be a generic system-level safety analysis tool for advanced non-LWRs, including Liquid-Metal-cooled fast Reactors (LMR), Molten Salt Reactors (MSR), Fluoride-salt-cooled High-temperature Reactors (FHR), and High-Temperature Gas-cooled Reactors (HTGR). SAM takes advantage of advances in physical modeling, numerical methods, and software engineering to enhance its user experience and usability. It utilizes an object-oriented computational framework (MOOSE [6]), and its underlying meshing and finite-element library and linear and non-linear solvers, to leverage the modern advanced software environments and numerical methods.

The Fluoride Salt-Cooled High-Temperature Reactor (FHR) is an advanced reactor technology that provides enhanced economic competitiveness and enables the expansion of nuclear energy to include industrial process heat applications. FHR technology uses a novel combination of existing technologies to achieve unique levels of economy, safety, flexibility, modularity, and security for nuclear power production, including pebble-type high-temperature coated TRISO particle fuel, molten fluoride salt coolants, reactor cavity cooling system for passive decay heat removal, etc. This new design brings additional challenges in demonstrating appropriate safety margins under various design basis accidents during the license application process with the Nuclear Regulatory Commission (NRC).

The transient modeling and simulations of the UC Berkeley Mk1 PB-FHR using SAM started in 2016, with early results [7] shown below. The preliminary system thermal fluids simulation capabilities were demonstrated for FHR. Since then, the SAM code has been continuously improved to support FHR transient analysis, including work under collaboration projects between Argonne and Kairos Power (KP) in recent years on improving SAM and KP-SAM [8] code capabilities to support design scoping, safety optimization, and licensing support analyses of PB-FHR. The research and development activities include: SAM capability enhancements for specific key FHR phenomena such as salt freezing, tritium transport, thermal radiation with salt, etc.; generic code capability enhancements; performing code verification and validations; integrating uncertainty quantification (UQ) techniques in safety analyses; and raising the software quality rigor level for commercial-grade applications. This ongoing collaboration has significantly raised the SAM code's technical and commercial maturity level to enable the use of SAM to support FHR design analysis and licensing application [9].
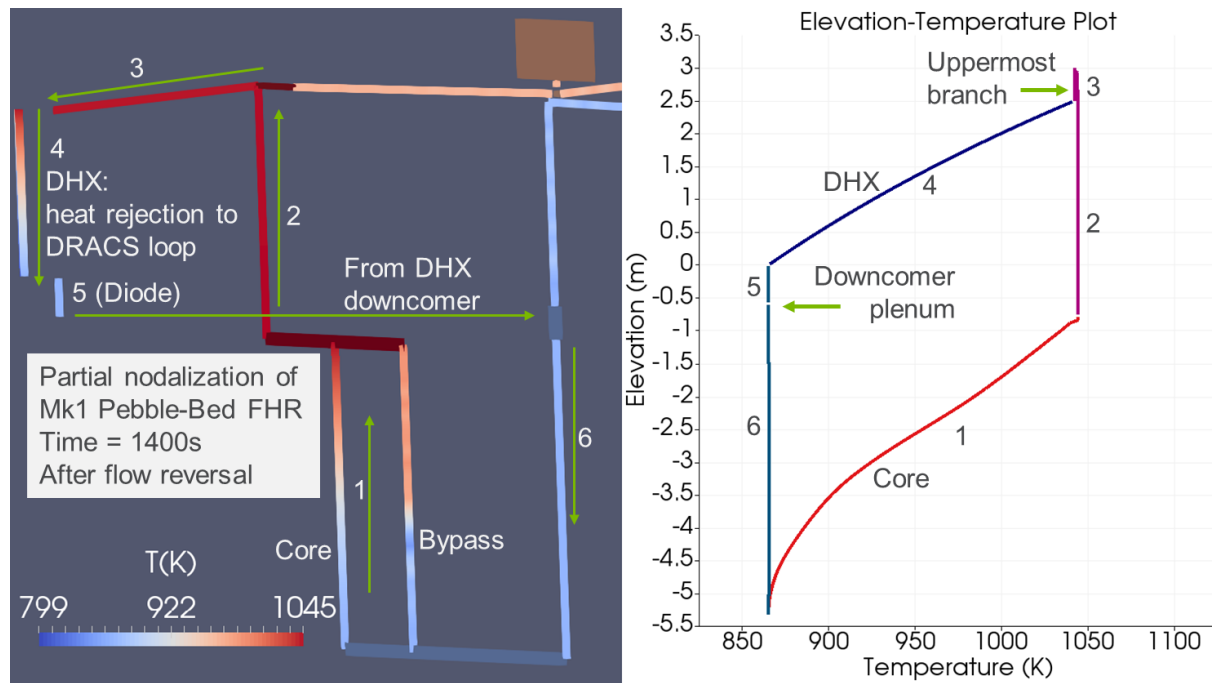
Figure 1-1. SAM simulation results of an FHR

Apart from the industry collaboration projects, DOE-NE's NEAMS program support is utilized in FY21 to improve code capabilities to support FHR transient analysis & validation. It supports the development of a reference plant model of a molten-salt cooled pebble bed reactor and simulation of loss of forced flow transient to address near-term NRC needs. The reference plant model is based on the UC Berkeley Mk1 PBFHR design with additional features from the KP-FHR design, which relies on reactor cavity cooling system concept for decay heat removal. Additionally, pebble bed modeling and closure models on pressure drop across pebble bed are improved in SAM; and additional code validations are performed using test data at the scaled FHR integral test facility CIET.

This report is organized as follows. Section 2 provides a brief description and verifications of SAM enhancements for pebble bed modeling including the spherical heat conduction and wall friction models of the pebble. Section 3 describes the reference FHR model development using SAM and the preliminary simulation results. Section 4 presents the updated CIET benchmark using the loss of flow test data. Lastly, a short summary and follow-up work are discussed in Section 5.

2   SAM Enhancements for FHR modeling

As discussed in Section 1, SAM has been developed to provide system-level modeling capability for advanced non-LWR safety reactor analysis. With advancements in reactor designs also come modeling challenges in capturing the varied geometries in those designs. Spherical pebble beds are a common element across these advanced reactor core designs, including both HTGRs and FHRs. In prior work, a porous medium flow model capability was incorporated into SAM's multi-dimensional flow model to allow for modeling of complex, but regular-patterned flow geometries such as a pebble bed [10]. In this work, a similar approach is taken to incorporate aspects of the porous medium flow model into the existing system-level 1-D flow and heat transfer model. The implementation of this model is discussed in Section 2.1. Empirical correlations for physical closure models specifically for packed bed flows were also previously incorporated into the SAM unified porous medium multi-dimensional flow model [11]. An extension of the wall friction correlations into the 1-D flow model is discussed in Section 2.2.

2.1 Spherical Geometry Core Channel Reduced Order Model

In SAM, a system-level modeling approach allows for flexible modeling of 1D fluid flow with coupled conjugate heat transfer to 1-D or 2-D solid heat-conducting structures [1]. A spherical geometry modeling capability is supplemented to the existing heat conduction and convective heat transfer model in Cartesian and cylindrical coordinates. The governing equation for thermal conduction in 1-D spherical geometry is given below:

$$\rho C_p \frac{\partial T}{\partial t} - \frac{1}{r^2}\frac{d}{dr}\left(kr^2\frac{dT}{dr}\right) - Q''' = 0 \tag{1}$$

where k is the thermal conductivity and Q''' is the volumetric internal heat source in the solid. This heat transfer model has been incorporated into the basic *HeatStructure* SAM component in 1-D, meaning that heat transfer is explicitly modeled symmetrically in the radial direction without considering heat transfer in the axial direction. In this way, the assumption for a randomly packed bed is that the pebbles are uniformly distributed throughout the solid domain and the *HeatStructure* component resembles a "stack" of representative spherical pebbles. Each axial element "layer" of the *HeatStructure* component is an average representation of all pebbles within the bounds of that axial layer, while maintaining the correct modeling of the total solid volume and surface area between the fluid and the solid.

In the fluid, SAM models 1-D single-phase flow as governed by the following equations:

$$\frac{\partial \rho}{\partial t} + \frac{\partial(\rho u)}{\partial t} = 0 \tag{2}$$

$$\rho\frac{\partial u}{\partial t} + \rho u\frac{\partial u}{\partial z} = -\frac{\partial p}{\partial z} - \rho g - \frac{f}{D_h}\frac{\rho u|u|}{2} \tag{3}$$

$$\rho C_p\frac{\partial T}{\partial t} + \rho C_p u\frac{\partial T}{\partial z} = q''' \tag{4}$$

where the fluid flow is modeled as a separate domain from the solid structure. In a representative pebble bed model, the fluid component simulates only the pore space region in the porous flow medium (i.e. $A_{cross-section} = \epsilon\, A_{bed}$, where ϵ is porosity). Therefore, the 'superficial' velocity v defined as $v = \epsilon\, u$ becomes the intrinsic velocity u as modeled in the governing equations.

Between the fluid and solid domain, conjugate heat transfer is modeled as a convective heat flux with the solid surface defined by the following equation:

$$q'' = -\frac{1}{r^2}\frac{d}{dr}\left(kr^2\frac{dT}{dr}\right) = h(T_{wall} - T_{bulk}) \tag{5}$$

in which h is the heat transfer coefficient and T_{wall} & T_{bulk} are the fluid temperatures at the wall and bulk, respectively. In the fluid domain, the convective heat flux is modeled as an additional heat source in the energy conservation equation

$$q''' = h(T_{wall} - T_{bulk})\frac{P_{heated}}{A_{flow}} = a_w h(T_{wall} - T_{bulk}) \tag{6}$$

in which P_{heated} is the heated perimeter, A_{flow} is the cross-sectional flow area, and a_w is the heat transfer surface area density which is equivalent to the ratio of the heated perimeter and the flow area. In the PBCoreChannel SAM component, the porosity ϵ is specified to calculate the total volume of the solid domain and the heat transfer surface area density a_w is specified to calculate the total surface area between the fluid and solid.

2.1.1 Verification of a horizontal pebble bed channel with analytical solution

To verify the implementation of the spherical geometry heat conduction model in the *HeatStructure* and *PBCoreChannel* SAM components, two verification cases are presented here. In the first case, a simple horizontal pebble bed channel with constant boundary conditions and volumetric heat generation in the solid is modeled to demonstrate conservation of energy balance across the channel and is based on a verification case previously used to demonstrate the explicit pebble temperature model in the multi-dimensional flow SAM model [12]. As discussed in the previous section, the fluid and solid domains are modeled as separate domains and the setup for this verification case is given below in Table 2-1 and Figure 2-1.

Table 2-1. Horizontal pebble channel verification problem setup.

Parameter	Value
Channel length [m]	1.0
Channel diameter [m]	0.01
Flow area (pore space) [m^2]	4.712 ×10^{-3}
Porosity ϵ	0.6
Pebble diameter [m]	0.06
Inlet temperature [K]	630
Inlet (superficial) velocity [m/s]	0.6
Outlet pressure [Pa]	1.0 ×10^5
Pebble volumetric heat source [W/m^3]	1.0 ×10^6
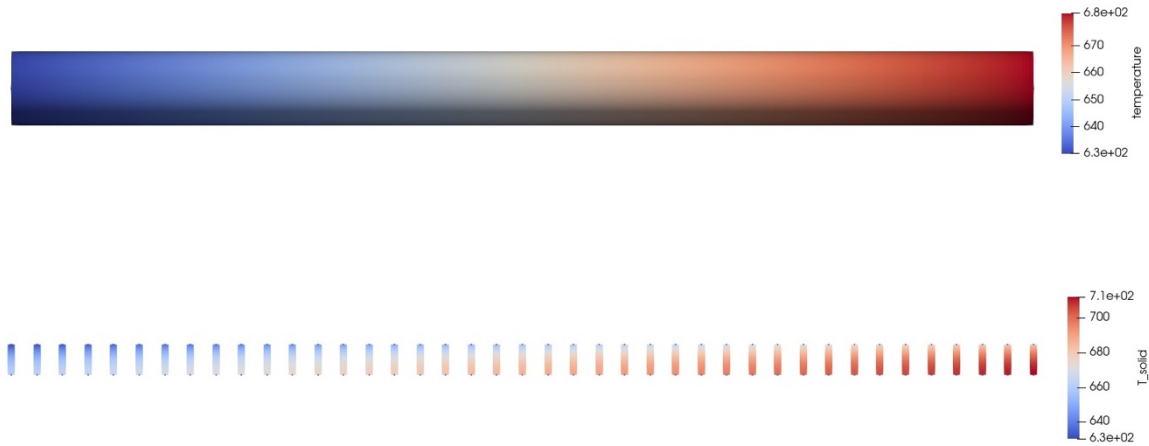
Figure 2-1. Horizontal pebble bed channel verification model with fluid domain (top) and averaged "stacked" spherical pebble solid domain (bottom) and simulated temperature profiles.

In this scenario, since convective heat transfer from the solid pebbles to the fluid is the only mechanism for heat transfer, the fluid bulk temperature should exhibit a linear increase from the inlet to the outlet, given that the fluid has a constant specific heat capacity. This bulk temperature can be analytically derived as:

$$T_f(x) = T_{in} + \frac{(1-\epsilon)q'''x}{\rho_{in}v_{in}C_p} \qquad (7)$$

In this verification case, the inlet fluid density $\rho_{in} = 77 \ kg/m^3$ and the fluid specific heat capacity $C_p = 100 \ J/kg - $K. Furthermore, if the pebble thermal conductivity $k = 5.0 \ W/m - $K and volumetric heat source $q''' = 10^6 \ W/m^3$ are both constant, the pebble radial temperature distribution at steady state can be analytically derived using the pebble surface temperature T_{ps} as a boundary condition. Assuming that the convective heat transfer is sufficiently large, we can use the outlet bulk fluid temperature as derived in equation (8) for our pebble surface temperature in the equation below:

$$T(r) = T_{ps} + \frac{q'''}{6k}(R^2 - r^2) \qquad (8)$$

This verification case was simulated as a steady state problem in SAM with 20 axial elements in the fluid and solid domains and 20 radial elements in the solid domain. The plots below in Figure 2-2 demonstrate nearly exact agreement between the numerical solution and the analytical solutions derived in Equations (7) and (8) for the bulk fluid temperature over the axial length (left) and the radial pebble temperature profile at the outlet (right).
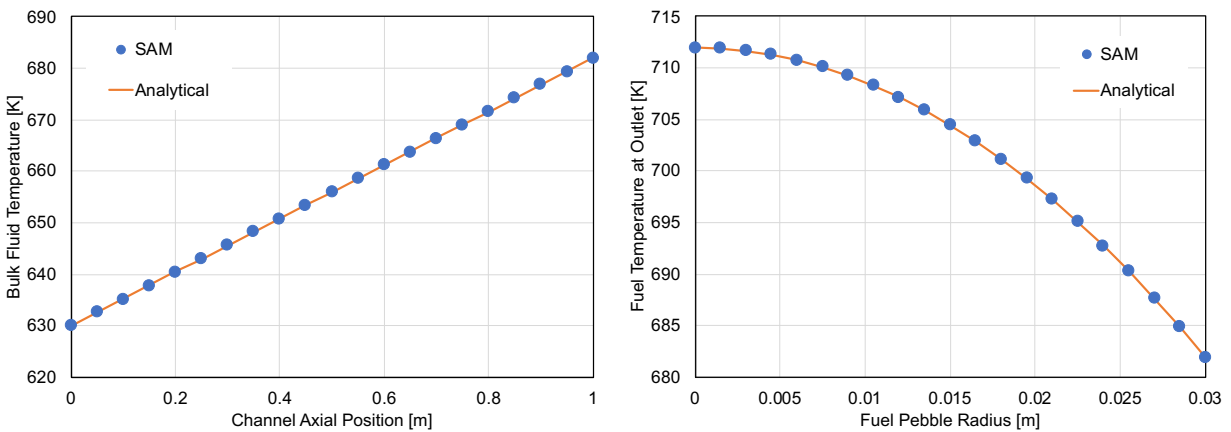
Figure 2-2. Verification of horizontal pebble bed channel, comparing predicted axial bulk fluid temperature (left) and predicated radial pebble temperature at the outlet (right) to analytical solutions.

Further analysis is performed through a mesh refinement study to verify the expected convergence of both temperature distributions using 5, 10, 20, and 40 elements in the radial and axial dimensions. In this SAM model, second-order elements and methods are used in both the fluid and solid domain meshes. In the plots below in Figure 2-3, we observe the expected second-order spatial accuracy in both the axial fluid temperature and the radial pebble temperature profiles.
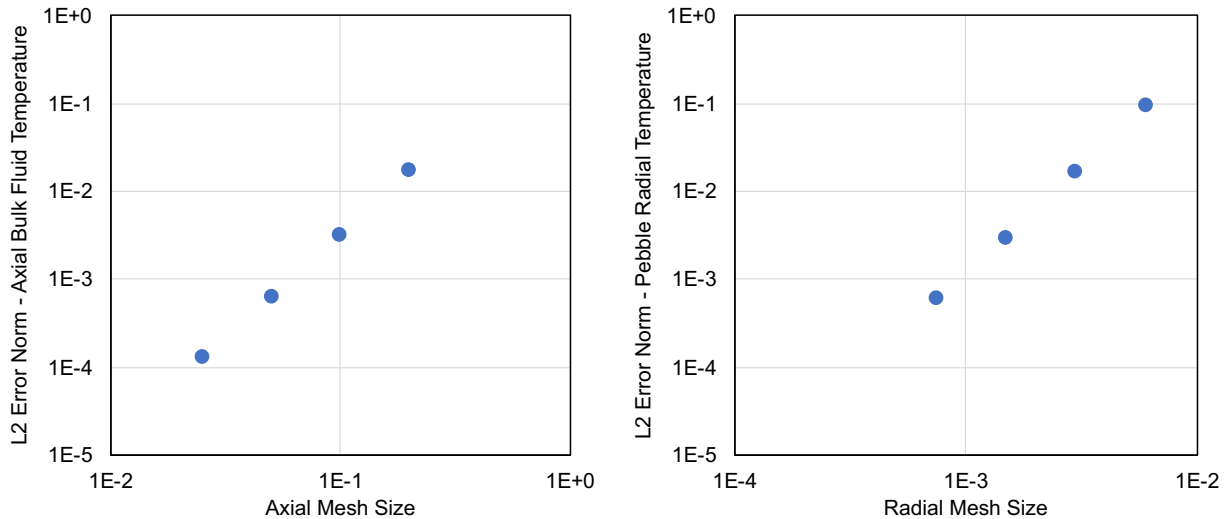
Figure 2-3. Mesh refinement study of the horizontal pebble bed core channel verification problem. Both the simulated axial bulk fluid temperature and outlet pebble radial temperature profiles demonstrate the expected 2nd order spatial convergence.

2.1.2   Verification of FHR reference core model in cylindrical and spherical geometry

The initial modeling of the FHR reference model represents the pebble bed core region using a cylindrical geometry for the fuel with 'fuel rods' analogous to a stack of pebbles. The pebble layer radii are adjusted to conserve the total pebble volume, using a scaling factor to achieve the correct total surface area. This model is described in further detail in Section 3.1. The objective of the present spherical geometry core channel model is to eliminate the need for such geometrical adjustments and improve the accuracy of the heat conduction modeling in the pebble bed. A verification case was developed to demonstrate this capability by performing a steady-state simulation of the active core region with specified constant inlet/outlet boundary conditions in both 1-D cylindrical and spherical solid domain geometries. In both cases, a single *PBCoreChannel* component is used to represent the entire core region with *PBTDJ/PBTDV* components applying the inlet/outlet boundary conditions for the fluid-flow through the active core. These boundary conditions were determined from the steady-state results of the full system SAM simulation model described in Section 3.1. The model parameters for the 1-D cylindrical and spherical geometry cases are compared below in Table 2-2.

Table 2-2. Comparison of SAM model parameters of the
FHR reference core model verification test.

Parameter	Cylindrical	Spherical
Active core height [m]	3.1	
Flow area (pore space) [m^2]	1.809557368	
Porosity ϵ	--	0.4
Pebble diameter [m]	0.01633	0.02
Hydraulic diameter [m]	0.04	
Heated diameter [m]	0.01778	
Heat transfer surface area density [m^2/m^3]	183.71	225
HTC scaling factor [SC_HTC]	1.225	1.0
Core power [MW]	320	
Inlet temperature [K]	823.33	
Inlet (superficial) velocity [m/s]	0.4812	
Outlet pressure [Pa]	3.944 $\times 10^5$	

Both reference core models are simulated as null transients from -1000 to 0 sec to achieve a steady-state condition in the core. From the results shown in Figure 2-4, conservation of the overall flow and heat transfer is achieved between the two models. The energy balance in the fluid from the core inlet to outlet converges to the total core power of 320 MW. The pressure drop in both models are expected to be equivalent as the fluid modeling is identical in both cases and separate of the solid domain modeling.

The steady state temperature profiles at the end of the null transient are shown in Figure 2-5. In comparing the two modeling cases, the bulk fluid temperature and averaged pebble surface temperature are identical, demonstrating consistent convective heat transfer modeling between the spherical model and the approximated cylindrical model. Upon examination of the radial

temperature profile, it is noted that the spherical pebble geometry represents the actual radii of each pebble layer, whereas the cylindrical model radii are scaled slightly smaller to preserve the total volume. As a result of the geometric model differences, the predicted pebble center temperature is about 20 K lower for the spherical model at the core midplane. Overall, this verification case and preliminary modeling effort demonstrates a good agreement between the conservativeness of the representative "cylindrical" pebble bed core model and an improved accuracy gained from the implemented spherical geometry model.
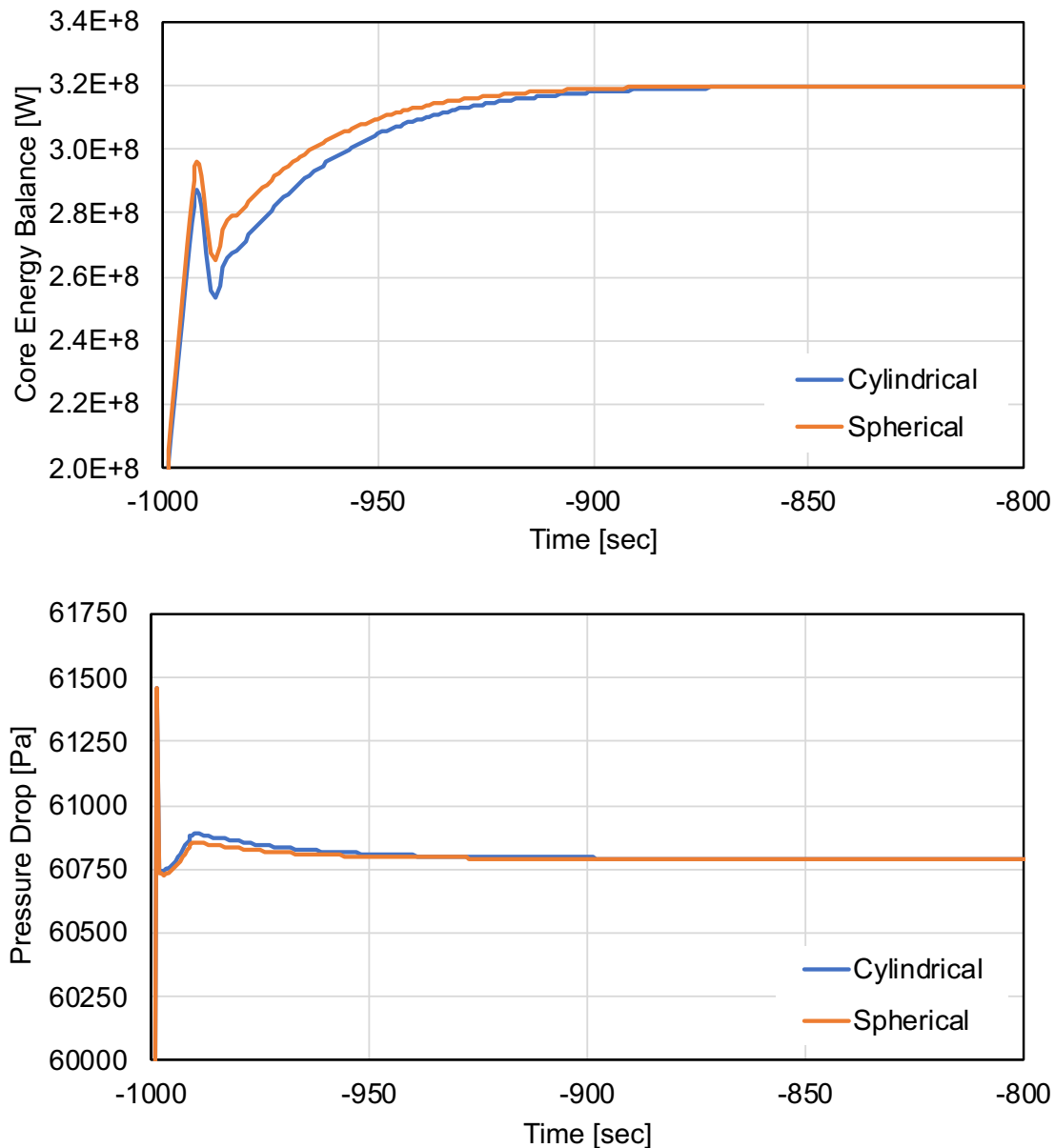
Figure 2-4. Comparison of steady-state convergence of total energy balance (top) and pressure drop (bottom) across the active core.
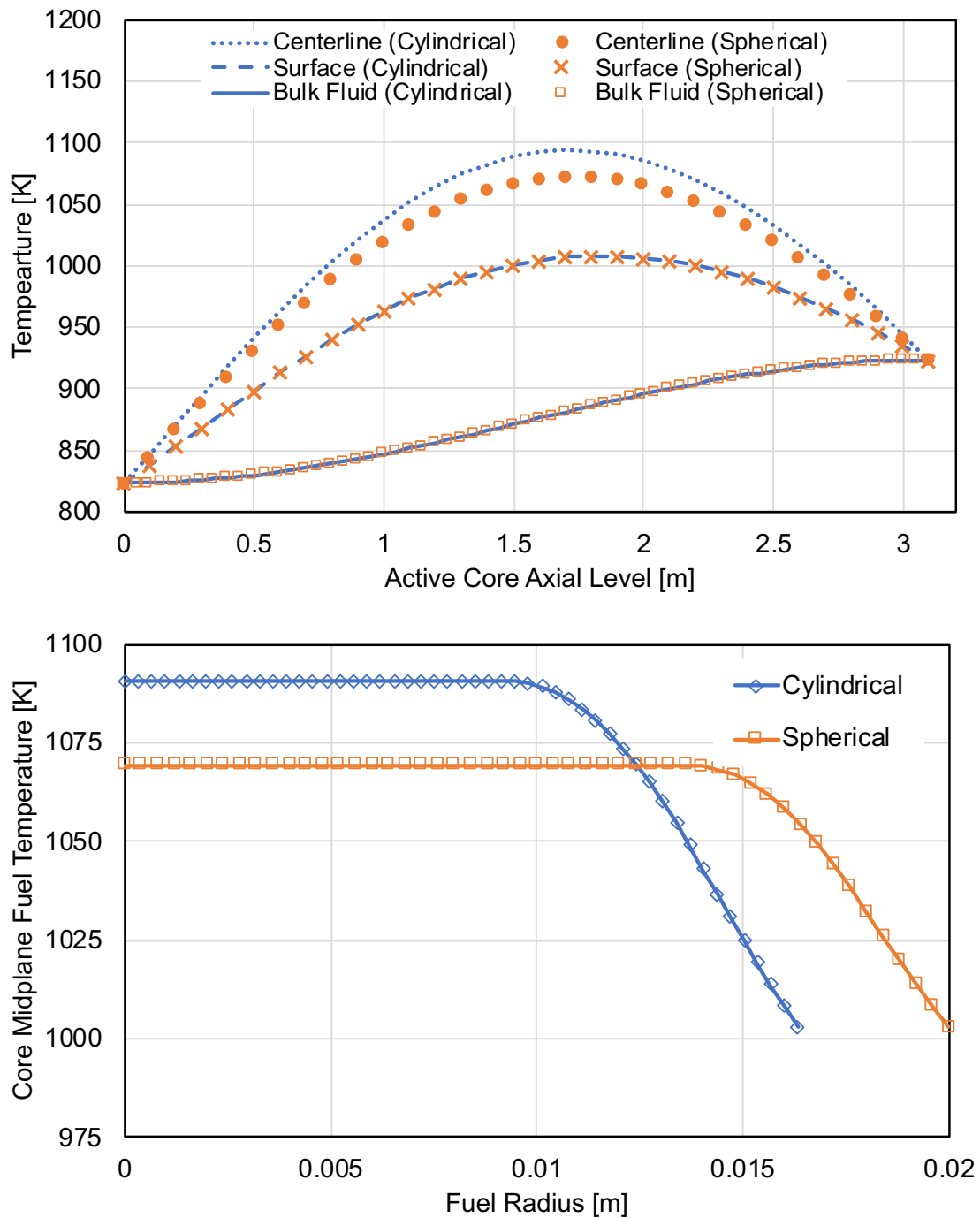
Figure 2-5. Comparison of axial average axial temperatures (top) and the average pebble radial temperature profile (bottom) at the core midplane (z = 1.55 m)

2.2 Wall Friction Models for Packed Bed Flow

In line with modeling spherical geometry heat transfer through the pebble bed, it is also important to consider the complex transport path of the fluid and its impact on the frictional pressure drop. The measurement and modeling efforts of packed bed flows has been well studied in the field of chemical engineering with some efforts made in the field of nuclear engineering as well. Prior efforts in SAM implemented a set of selected empirical correlations from literature that are well-suited or well-known for modeling packed bed flows in nuclear reactor designs into the porous flow multidimensional flow model [11]. The current work extends these correlations into the 1-D fluid flow model to support our modeling of 1-D system models with pebble beds.

In the fluid momentum conservation described in Equation (2), the pressure drop attributed to wall friction is described by the last term in the equation, modeling the Darcy-Weisbach equation by using the dimensionless Darcy friction factor f:

$$\frac{\Delta p}{L} = -\frac{f}{D_h}\frac{\rho u|u|}{2} \tag{9}$$

In randomly packed beds, the non-dimensional friction factor is often represented as Ψ with the following relation for the pressure drop as defined in several empirical correlations:

$$\frac{\Delta p}{L} = \Psi\frac{1-\epsilon}{\epsilon^3}\frac{1}{d_p}\frac{\rho v^2}{2} \tag{10}$$

in which ϵ is the porosity, d_p is the pebble diameter, and v is the superficial velocity. The friction factor Ψ is given as a function of the modified Reynolds number Re_m:

$$\text{Re}_m = \frac{\rho v d_p}{\mu(1-\varepsilon)} \tag{11}$$

Since our 1-D fluid domain only considers the pore space flow area, in the governing equations the superficial velocity is modeled as the intrinsic velocity ($u = v$), allowing the Darcy friction factor to be related to the non-dimensional packed bed friction factor Ψ as shown below in Equation (12). This allows us to use the porous flow friction correlations in the 1-D fluid model.

$$f = \Psi\frac{D_h}{d_p}\frac{1-\epsilon}{\epsilon^3} \tag{12}$$

Three empirical correlations were selected to model porous flow friction in the multidimensional model and are incorporated here in the 1-D fluid model. The first correlation was developed by Ergun [13] and was derived from 640 experimental data points of measured pressure drop through spheres, sand, and pulverized coke of varying sizes and fluids to provide the following correlation:

$$\Psi_{Ergun} = \frac{300}{\text{Re}_m} + 3.5 \tag{13}$$

The Ergun correlation was derived from data over the range of $1 \leq \text{Re}_m \leq 2500$. This is a prevalent correlation in thermal-hydraulics modeling of pebble bed designs and was included for its familiarity to code users.

The second correlation was developed by the Nuclear Safety Standards Commission of Germany (KTA) [14] as part of a large-body effort to develop thermal-hydraulic correlations to support the HTGR modeling effort. The KTA correlation was developed from a review of published data and correlations from roughly 30 papers and is given as:

$$\Psi_{KTA} = \frac{320}{\text{Re}_m} + \frac{6}{\text{Re}_m^{0.1}} \tag{14}$$

The KTA correlation was determined to be valid over the range of $1 < \text{Re}_m < 10^5$, for a bed porosity of $0.36 < \epsilon < 0.42$ and for bed height/pebble diameter ratios of $L/d_p > 5$. The minimum diameter ratio of the pebble bed to pebble diameter is also given as a function of the modified Reynolds number (see [14]). This correlation was determined to have an uncertainty of $\pm 15\%$ with a confidence level of 95%.

The third correlation was developed by Eisfeld and Schnitzlein [15] to determine the influence of the container wall on the packed bed pressure drop. From reviewing 24 correlations incorporating over 2300 data points, they adopted the methodology proposed by Reichelt [16] to account for this effect. For randomly packed spherical particles, the developed correlation incorporated the bed diameter D_{bed} as a parameter:

$$\Psi_{Eisfeld-Schnitzlein} = \frac{308A_w^2}{\text{Re}_m} + \frac{2A_w}{B_w} \tag{15}$$

$$A_w = 1 + \frac{2\left(d_p/D_{bed}\right)}{3(1-\epsilon)} \tag{16}$$

$$B_w = \left[1.15\left(\frac{d_p}{D_{bed}}\right)^2 + 0.87\right]^2 \tag{17}$$

This correlation was determined from data over the range of $0.01 < \text{Re}_{d_p} < 17535$, where $\text{Re}_{d_p} = \rho u d_p / \mu$. The correlation is valid for a porosity of $0.330 < \epsilon < 0.882$ and for a diameter ratio of $1.624 \leq D_{bed}/d_p \leq 250$, with an RMS error of $\sigma = 0.1613$. All three of these correlations have been implemented as model options in the 1-D fluid model available to users.

2.2.1 Verification and validation of 1-D packed bed friction correlations with the TAMU pressure drop experiment

In order confirm the correct implementation of these correlations, a previous validation test performed using the SAM multidimensional flow model [11] to model a set of experiments from the Texas A&M University (TAMU) pressure drop test facility is used to provide both code-to-code verification and validation of the 1-D packed bed flow pressure drop correlations. The TAMU test facility was setup to perform experiments on single-phase flow pressure drop in packed beds. The apparatus is constructed of a cylindrical column with randomly packed spherical beads, with all components composed of a transparent polymethyl methacrylate (PMMA) [17]. The test facility can use both air and water as the working fluid and implemented varying sizes of spherical beads (pebbles) throughout the experiment (see Table 2-3).

Table 2-3. Dimensions of test section of TAMU water/air pressure drop experiment

Bed height, L (cm)	Bed diameter, D (cm)	Particle diameter, d_p (cm)	D/d_p [-]	Bed porosity [-]
152.4	12.065	0.635	19	0.385
		1.27	9.5	0.397
		1.905	6.33	0.416
		3.302	3.65	0.465
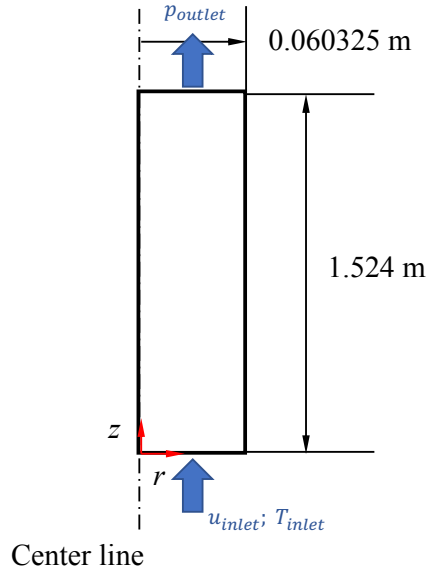
Figure 2-6. Diagram of modeled domain of the TAMU pressure drop experiment with dimensions and boundary conditions [11].

The 1-D flow SAM model was developed to be consistent with the multidimensional (2-D) flow validation model, using a *PBOneDFluidComponent* to model the fluid region in the test section. A *PBTDJ* component was used to apply inlet boundary conditions, for which the inlet temperature was assumed to be 30 °C and inlet velocity was set to the experiment inlet superficial velocities (see Table 2-4 and Table 2-5). A *PBTDV* component was used to apply the outlet boundary condition, which assumed the system pressure to be at atmospheric pressure, 10^5 Pa. The 1-D flow model implemented the same equation of state model for consistent fluid properties.

Table 2-4. Selected conditions for SAM simulations on TAMU water test cases

d_p = 6.35 mm D/d_p = 19		d_p = 12.7 mm D/d_p = 9.5		d_p = 19.05 mm D/d_p = 6.33		d_p = 33.02 mm D/d_p = 3.65	
Inlet superficial velocity (m/s)	Re_m	Inlet superficial velocity (m/s)	Re_m	Inlet superficial velocity (m/s)	Re_m	Inlet superficial velocity (m/s)	Re_m
0.05	6.4465E+02	0.1	2.6299E+03	0.1	4.0732E+03	0.1	7.7069E+03
0.1	1.2893E+03	0.2	5.2599E+03	0.2	8.1465E+03	0.2	1.5414E+04
0.2	2.5786E+03	0.3	7.8898E+03	0.3	1.2220E+04	0.3	2.3121E+04
0.25	3.2233E+03	0.4	1.0520E+04	0.4	1.6293E+04	0.4	3.0828E+04

Table 2-5. Selected conditions for SAM simulations on TAMU air test cases

d_p = 6.35 mm D/d_p = 19		d_p = 12.7 mm D/d_p = 9.5		d_p = 19.05 mm D/d_p = 6.33	
Inlet superficial velocity (m/s)	Re_m	Inlet superficial velocity (m/s)	Re_m	Inlet superficial velocity (m/s)	Re_m
0.4	2.6387E+02	0.4	5.3823E+02	0.4	8.3362E+02
0.6	3.9580E+02	0.8	1.0765E+03	0.8	1.6672E+03
0.8	5.2773E+02	1.2	1.6147E+03	1.2	2.5008E+03
1.0	6.5966E+02	1.6	2.1529E+03	1.6	3.3345E+03
1.2	7.9160E+02	2.0	2.6912E+03	2.0	4.1681E+03
		2.4	3.2294E+03	2.4	5.0017E+03
		2.8	3.7676E+03	2.8	5.8353E+03
		3.2	4.3059E+03	3.2	6.6689E+03
		3.6	4.8441E+03	3.6	7.5025E+03
		4.0	5.3823E+03	4.0	8.3362E+03

Steady state simulations were performed with the 1-D flow SAM model and compared with the multi-dimensional flow (2-D) SAM model for all selected conditions for both the air and water test cases. The three correlations for pressure drop were applied and the results of both code models were compared with the experimental data. The results are plotted in Figure 2-7 and Figure 2-8.
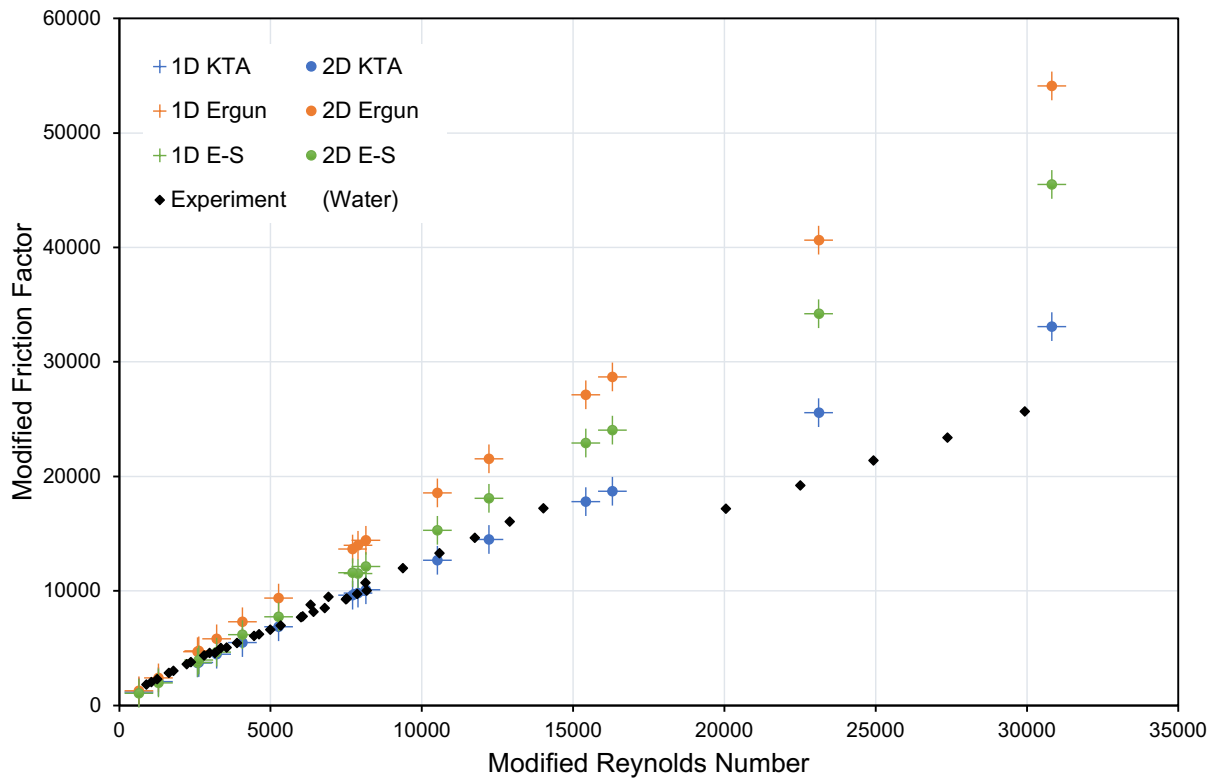
Figure 2-7. Comparison of predicted pressure drop using the 1-D and multidimensional (2-D) SAM model with the measured TAMU facility experimental data from tests with water.
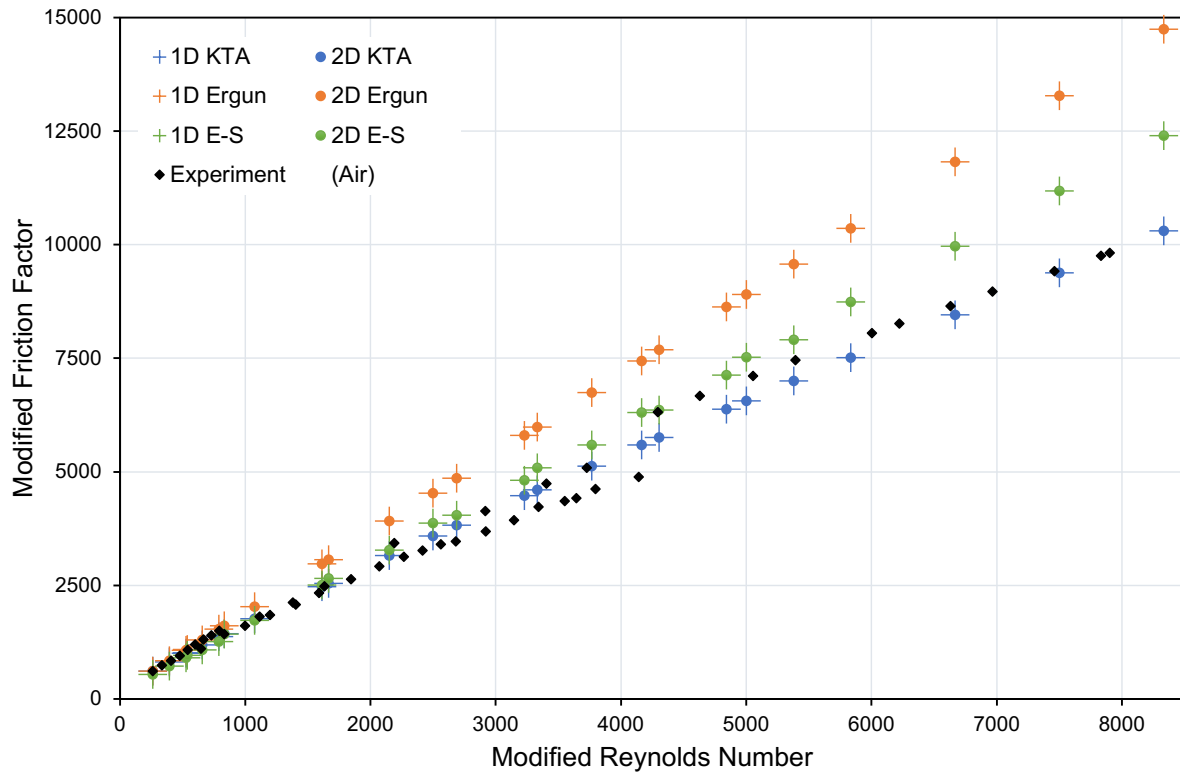
Figure 2-8. Comparison of predicted pressure drop using the 1-D and multidimensional (2-D) SAM model with the measured TAMU facility experimental data from tests with air.

The predicted pressure drops of the 1-D and 2-D SAM models yielded practically the exact same result as shown by the plots, which is an expected confirmation as the model is setup in a consistent manner. The comparison of the two models is further detailed in Table 2-6 and Table 2-7, demonstrating an agreement between the results to 5 significant figures over the range of conditions and for all three correlations.

With regards to validation with the experimental results, the same conclusions hold as previously assessed with the 2-D model validation. In most cases and conditions, the KTA correlation exhibited the best agreement to the test data, with the Ergun and Eisfeld-Schnitzlein correlations overpredicting the friction factor as the modified Reynolds number increased. For the set of water test cases with $D_{bed}/d_p = 3.65$, none of the correlations demonstrated good agreement with the data, likely due to the diameter ratio being too small. From these results, the KTA correlation has been implemented as the default correlation when a pebble bed geometry is selected for 1-D fluid flow in SAM.

Table 2-6. Comparison of predicted friction factors between the 1-D and multidimensional (2-D) SAM model for selected modified Reynolds numbers from the TAMU water tests [11].

u_{inlet}	Re_m	KTA		Ergun		Eisfeld and Schnitzlein	
		1-D SAM	2-D SAM	1-D SAM	2-D SAM	1-D SAM	2-D SAM
			d_p = 6.35 mm; D/d_p = 19				
0.05	6.4465E+02	1.1728E+03	1.1728E+03	1.2781E+03	1.2781E+03	1.0658E+03	1.0658E+03
0.1	1.2893E+03	2.0499E+03	2.0499E+03	2.4063E+03	2.4063E+03	1.9595E+03	1.9595E+03
0.2	2.5786E+03	3.6867E+03	3.6867E+03	4.6626E+03	4.6626E+03	3.7470E+03	3.7470E+03
0.25	3.2233E+03	4.4711E+03	4.4711E+03	5.7907E+03	5.7907E+03	4.6408E+03	4.6408E+03
			d_p = 12.7 mm; D/d_p = 9.5				
0.1	2.6299E+03	3.7498E+03	3.7498E+03	4.7524E+03	4.7524E+03	3.9597E+03	3.9597E+03
0.2	5.2599E+03	6.8588E+03	6.8588E+03	9.3548E+03	9.3547E+03	7.7275E+03	7.7275E+03
0.3	7.8898E+03	9.8090E+03	9.8090E+03	1.3957E+04	1.3957E+04	1.1495E+04	1.1495E+04
0.4	1.0520E+04	1.2660E+04	1.2660E+04	1.8560E+04	1.8560E+04	1.5263E+04	1.5263E+04
			d_p = 19.05 mm; D/d_p = 6.33				
0.1	4.0732E+03	5.4819E+03	5.4819E+03	7.2782E+03	7.2782E+03	6.1672E+03	6.1672E+03
0.2	8.1465E+03	1.0091E+04	1.0091E+04	1.4406E+04	1.4406E+04	1.2120E+04	1.2120E+04
0.3	1.2220E+04	1.4465E+04	1.4465E+04	2.1535E+04	2.1535E+04	1.8073E+04	1.8073E+04
0.4	1.6293E+04	1.8692E+04	1.8692E+04	2.8663E+04	2.8663E+04	2.4025E+04	2.4025E+04
			d_p = 33.02 mm; D/d_p = 3.65				
0.1	7.7069E+03	9.6074E+03	9.6073E+03	1.3637E+04	1.3637E+04	1.1582E+04	1.1582E+04
0.2	1.5414E+04	1.7790E+04	1.7790E+04	2.7124E+04	2.7124E+04	2.2887E+04	2.2887E+04
0.3	2.3121E+04	2.5554E+04	2.5554E+04	4.0611E+04	4.0611E+04	3.4193E+04	3.4193E+04
0.4	3.0828E+04	3.3058E+04	3.3058E+04	5.4098E+04	5.4098E+04	4.5498E+04	4.5498E+04

Table 2-7. Comparison of predicted friction factors between the 1-D and multidimensional (2-D) SAM model for selected modified Reynolds numbers from the TAMU air tests [11].

u_{inlet}	Re_m	KTA		Ergun		Eisfeld and Schnitzlein	
		1-D SAM	2-D SAM	1-D SAM	2-D SAM	1-D SAM	2-D SAM
			$d_p = 6.35$ mm; $D/d_p = 19$				
0.4	2.6387E+02	6.1325E+02	6.1325E+02	6.1179E+02	6.1179E+02	5.3789E+02	5.3789E+02
0.6	3.9580E+02	8.1289E+02	8.1289E+02	8.4265E+02	8.4265E+02	7.2081E+02	7.2081E+02
0.8	5.2773E+02	1.0059E+03	1.0059E+03	1.0735E+03	1.0735E+03	9.0370E+02	9.0370E+02
1	6.5966E+02	1.1940E+03	1.1940E+03	1.3044E+03	1.3044E+03	1.0866E+03	1.0866E+03
1.2	7.9160E+02	1.3784E+03	1.3784E+03	1.5353E+03	1.5353E+03	1.2695E+03	1.2695E+03
		$d_p = 12.7$ mm; $D/d_p = 9.5$					
0.4	5.3823E+02	1.0211E+03	1.0211E+03	1.0920E+03	1.0920E+03	9.6301E+02	9.6301E+02
0.8	1.0765E+03	1.7666E+03	1.7666E+03	2.0338E+03	2.0338E+03	1.7341E+03	1.7341E+03
1.2	1.6147E+03	2.4742E+03	2.4742E+03	2.9758E+03	2.9758E+03	2.5053E+03	2.5053E+03
1.6	2.1529E+03	3.1581E+03	3.1581E+03	3.9176E+03	3.9176E+03	3.2764E+03	3.2764E+03
2.0	2.6912E+03	3.8249E+03	3.8249E+03	4.8595E+03	4.8595E+03	4.0475E+03	4.0475E+03
2.4	3.2294E+03	4.4785E+03	4.4785E+03	5.8014E+03	5.8014E+03	4.8185E+03	4.8185E+03
2.8	3.7676E+03	5.1211E+03	5.1211E+03	6.7433E+03	6.7433E+03	5.5897E+03	5.5897E+03
3.2	4.3059E+03	5.7547E+03	5.7547E+03	7.6853E+03	7.6853E+03	6.3608E+03	6.3608E+03
3.6	4.8441E+03	6.3803E+03	6.3803E+03	8.6272E+03	8.6272E+03	7.1319E+03	7.1319E+03
4.0	5.3823E+03	6.9990E+03	6.9990E+03	9.5691E+03	9.5691E+03	7.9030E+03	7.9030E+03
		$d_p = 19.05$ mm; $D/d_p = 6.33$					
0.4	8.3362E+02	1.4364E+03	1.4364E+03	1.6089E+03	1.6089E+03	1.4330E+03	1.4330E+03
0.8	1.6672E+03	2.5418E+03	2.5418E+03	3.0676E+03	3.0676E+03	2.6510E+03	2.6510E+03
1.2	2.5008E+03	3.5908E+03	3.5908E+03	4.5265E+03	4.5265E+03	3.8692E+03	3.8692E+03
1.6	3.3345E+03	4.6047E+03	4.6047E+03	5.9853E+03	5.9853E+03	5.0875E+03	5.0875E+03
2.0	4.1681E+03	5.5932E+03	5.5932E+03	7.4441E+03	7.4441E+03	6.3058E+03	6.3058E+03
2.4	5.0017E+03	6.5622E+03	6.5622E+03	8.9029E+03	8.9029E+03	7.5240E+03	7.5240E+03
2.8	5.8353E+03	7.5149E+03	7.5149E+03	1.0362E+04	1.0362E+04	8.7423E+03	8.7423E+03
3.2	6.6689E+03	8.4541E+03	8.4541E+03	1.1821E+04	1.1821E+04	9.9606E+03	9.9606E+03
3.6	7.5025E+03	9.3816E+03	9.3816E+03	1.3279E+04	1.3279E+04	1.1179E+04	1.1179E+04
4.0	8.3362E+03	1.0299E+04	1.0299E+04	1.4738E+04	1.4738E+04	1.2397E+04	1.2397E+04

3   Development of a Reference FHR Model

In FY2020, a generic model was developed to demonstrate the ability of SAM to simulate the primary loop of a pebble-bed fluoride-salt-cooled, high temperature reactor (PB-FHR) [18]. The model was designed to be representative of a generic PB-FHR by building on the University of California, Berkeley (UCB) Mk1 design [19] and considering some of the publicly-shared features of early commercial designs. Shortly after the development of the generic SAM PB-FHR model, Kairos Power released the properties of a gFHR, which is meant to act as a benchmark [20]. The gFHR and the generic SAM PB-FHR share many common features, including the temperature rise across the core and downcomer geometry, but some of the key features of the reactor core, for example the pebble thickness, were different. In order to better align the SAM generic PB-FHR with the gFHR geometry, the core geometry was updated to use the gFHR geometry. Key changes are outlined in Table 3-1 and an updated representation of the reactor core is shown in Figure 3-1.
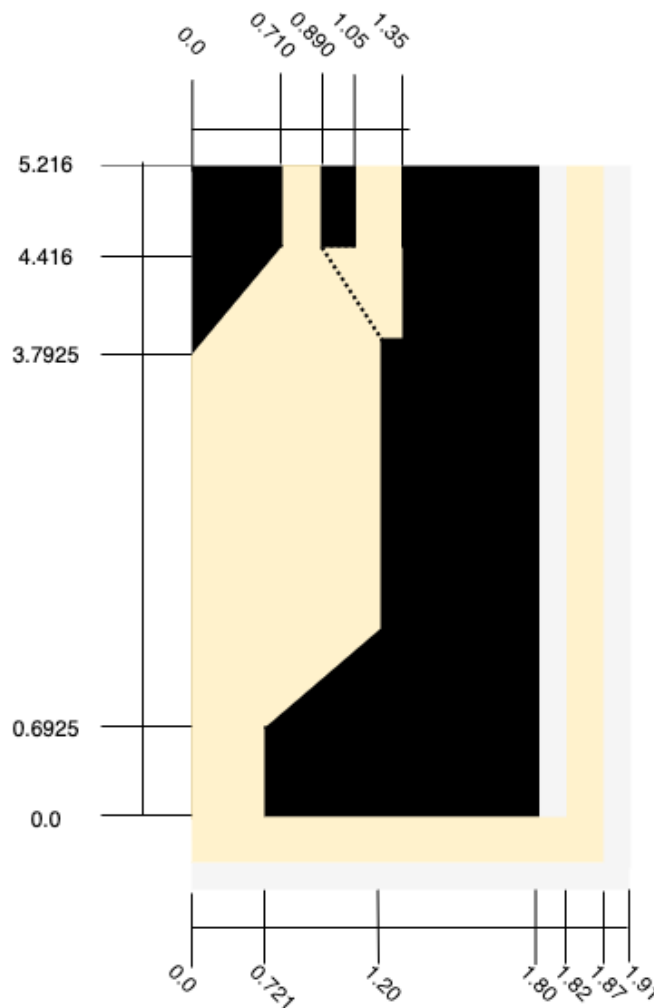

Figure 3-1. Updated dimensions of a generic PB-FHR reactor core.

Table 3-1. Differences between the gFHR and the SAM generic PB-FHR.

Property	PB-FHR	gFHR [20]
Power [MW]*	320	280
Core Radius [m]	1.05	1.2
Core Height [m]	2.5	3.1
Porosity [#]	0.4	0.4
Vessel Thickness [cm]	6	4
Downcomer Thickness [cm]	5	5
Mass Flow Rate [kg/s]*	1324.6	1173
Pebble Radius [cm]	1.5	2
Low Density Graphite Thickness [cm]	1.25	1.38
Fuel Layer Thickness [cm]	0.15	0.42
Shell Layer Thickness [cm]	0.1	0.2

* The PB-FHR power and flow rate were not updated to match the gFHR power and flow rate in order to avoid redesigning the PB-FHR heat exchangers.

In addition to updating the reactor core geometry, several updates were made to the generic PB-FHR. These updates include:

- the introduction of a fluid diode,

- detailed modeling of an intermediate loop,

- detailed modeling of a Reactor Cavity Cooling System (RCCS),

- explicit modeling of the heat transfer between the core reflector, core barrel and reactor vessel wall,

- point kinetics modeling,

- and decay heat modeling using the ANS standard ANSI/ANS-5.1-2005.

An updated representation of the generic PB-FHR can be found in Figure 3-2. Upon exiting the salt collection ring within the graphite reflector, the hot salt travels upwards, 1, where it exits the reactor vessel. The hot salt then passes the expansion tank, 2, and enters the primary coolant pump, 3. After exiting the pump, the hot salt passes through a helical heat exchanger, 4, where energy is transferred to "solar" salt, 7. The cooled salt then passes through a network of piping, 5, until it reaches the reactor vessel and is distributed within the downcomer, 6. The pipes that compose the primary system are assumed to be 24 in. Schedule 80 pipe. In order to prevent the primary salt velocity from exceeding 2 m/s, an identical second primary loop is introduced.

The fluid diode, 12, connects the extraction pipe, 1, to the downcomer, 6. When the primary pump is not running the fluid diode opens and allows for the flow of coolant from the extraction

pipe to the downcomer, establishing a flow path for natural circulation. When the primary pump is operating, the fluid diode closes and reduces the amount of bypass flow between the downcomer and the extraction pipe. Together with the RCCS, 10 and 11, the fluid diode allows for passive heat removal from the primary system.

The RCCS is connected to the primary loop through radiative heat transfer at the reactor vessel wall. The water within the RCCS picks up heat at guard vessel wall, 10, and rejects heat at the air dump heat exchanger, 11. The air dump heat exchanger is connected to an outlet stack in order to increase the natural circulation driving head. Due to the passive nature of the RCCS, heat loss occurs during normal and off-normal operation. The RCCS system in the generic PB-FHR was designed to remove the long-term decay heat of the system, or 0.5% of the full power. During normal operating conditions, this results in 0.2% heat loss to the environment.

The remaining 99.8% of the reactor power is transferred to the solar salt within the intermediate loop. The properties for the secondary salt, "solar" salt, were obtained from [21]. The primary salt is assumed to be on the tube side of the heat exchanger. There are 1208 primary tubes with an inner diameter of 1.96 cm and a total flow length of 18.47 m. The shell side of the heat exchanger has a length of 3.418 m and a flow area of 0.2 m^2. The "solar" salt enters the heat exchanger at 700.15 K with a mass flow rate of 5,060 kg/s. After exiting the helical heat exchanger, 7, the solar salt travels through a steam generator, 8, and intermediate pump, 9. The steam generator within the generic PB-FHR is designed to cool the solar salt, exiting the heat exchanger at 743 K, to 701 K. This is accomplished in the SAM model by using a convective heat transfer boundary condition at the outer wall of the intermediate loop where the steam generator would be located. During normal operation, the heat transfer coefficient is kept artificially high in order to ensure the solar salt exits the steam generator at 701 K.
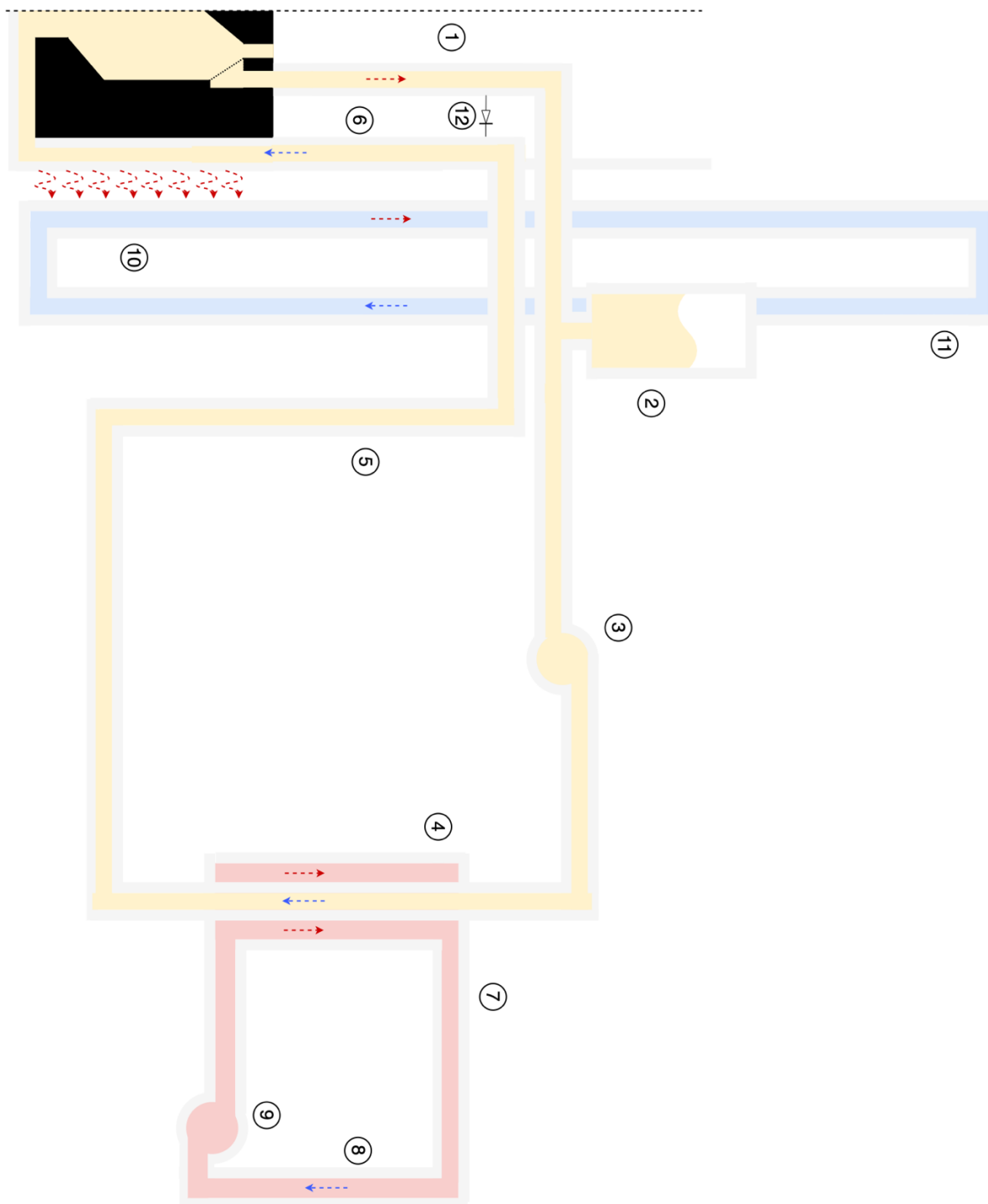
Figure 3-2. Graphical representation of the generic PB-FHR.

3.1 Generic PB-FHR Model Demonstration

Using the primary system geometry shown in Figure 3-2, two 1-D SAM models were developed. In the first model, a single average channel is used to represent the reactor core. In the second model, the reactor core is broken into 5 core channels of equal volume. For both models, the reactor core is discretized into 4 axial zones: the fueling chute, an expansion region, the active core and a contraction region. A sinusoidal power profile is assumed in the axial direction of the active core zone, and all power is assumed to be generated within the fuel layer of the pebble. The multi-channel model includes a radial power profile that approximates a Bessel function of the first order. The radial layout of each active core model is shown in Figure 3-3. Both models approximate the fuel pebbles using fuel rods by assuming that the fuel pebbles are stacked one on top of the other. The thickness of each region within the fuel rod are scaled down to conserve the mass of each pebble region. The total surface area for a stack of pebbles was conserved by scaling up the heat transfer coefficient by the ratio of the stacked pebble surface area to the cylindrical rod surface area. Intra-channel flow and heat transfer are not considered at this time.
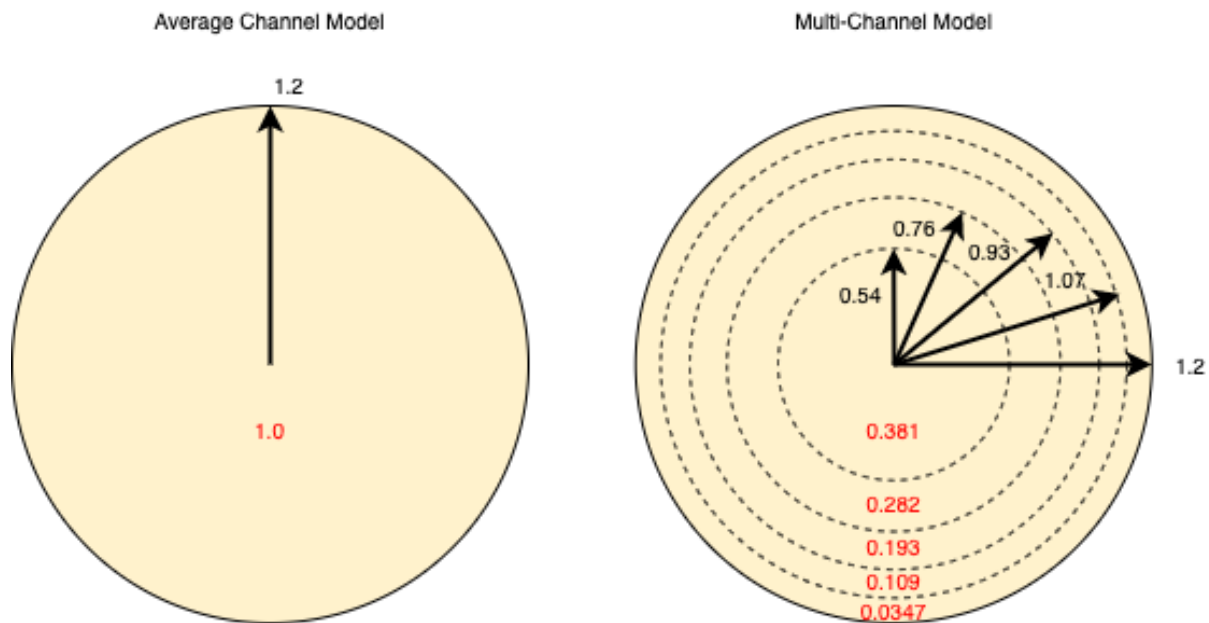
Figure 3-3. Active core layout in the average channel (left) and multi-channel (right) core model. Radial dimensions are in black and fractional radial power distribution is in red.

The remainder of the primary loop was modeled using a series of *PBPipe*, *PBBranch* and *PBVolumeBranch* components with a *PBPump* and *PBHeatExchanger* component. A single loop with a flow area scaled by a factor of two was used to represent the two-loop system in order to reduce the complexity of the model. The pump head was calibrated such that the flow rate within the primary system reached the steady state value of 1324.6 kg/s. A pump head of 0.30 MPa achieved this value. The steady state temperatures within the active zone of the core, coolant temperatures within the primary system, and coolant temperatures within the RCCS are shown in

Figure 3-4, Figure 3-5, Figure 3-6, respectively. Currently, SAM is not able to graphically represent a helical tube (while conserving the length and height of the helical tube), as a result the temperature profile shows a discontinuity at the end of the heat exchanger. This discontinuity is not present within the 1-D model and is simply an artifact of the visualization software.

Figure 3-4. Active core temperatures at steady state for the average channel (left) and multi-channel (right) model.

Figure 3-5. Primary loop coolant temperatures at steady state for both models.

Figure 3-6. RCCS temperatures at steady state. GV wall shown for scale.

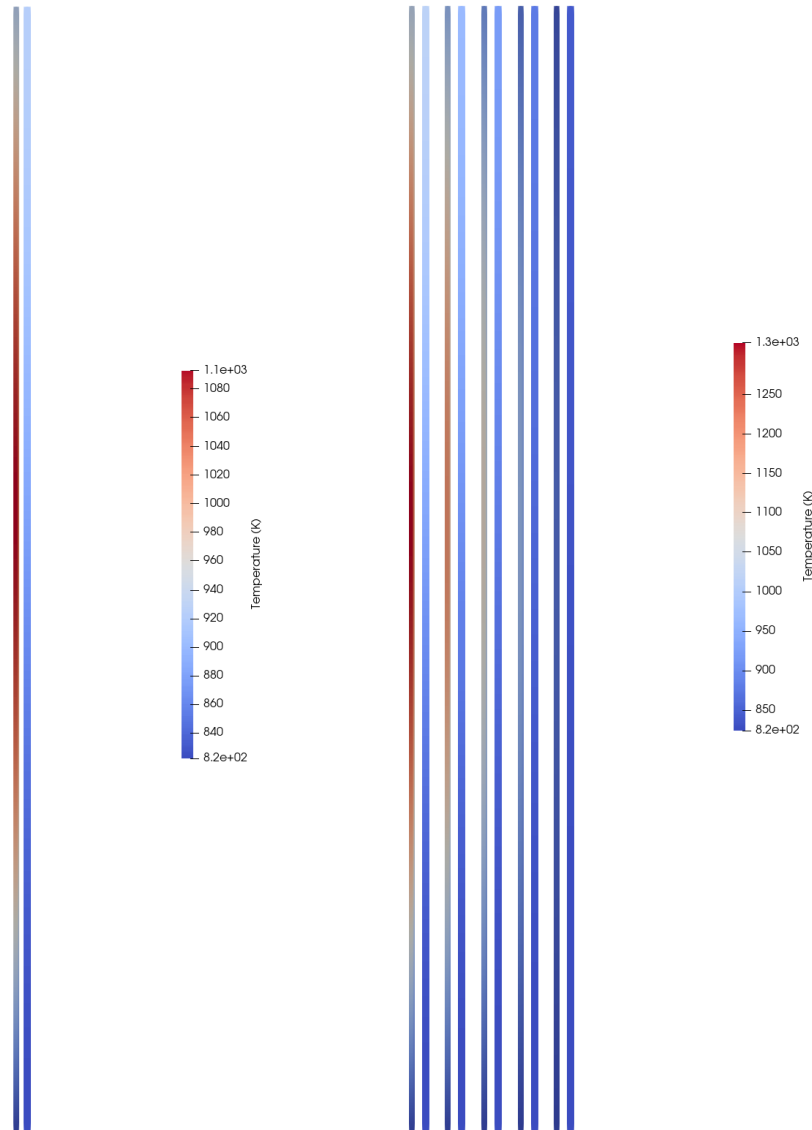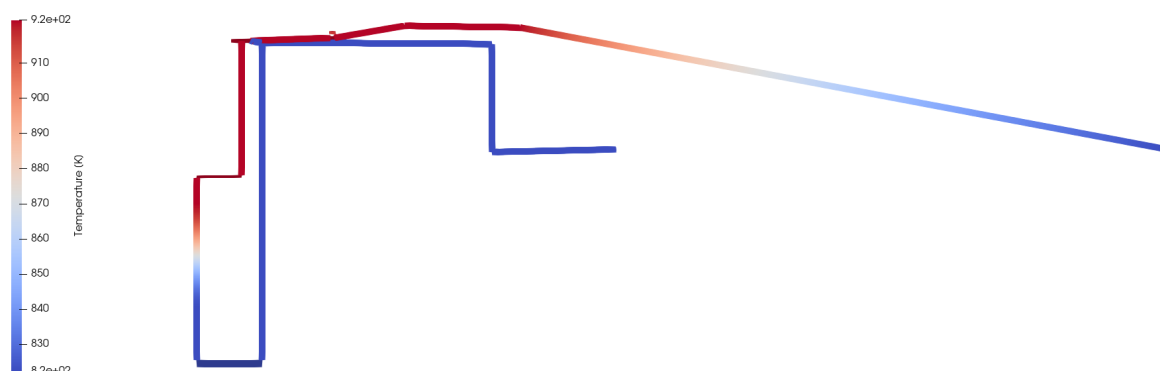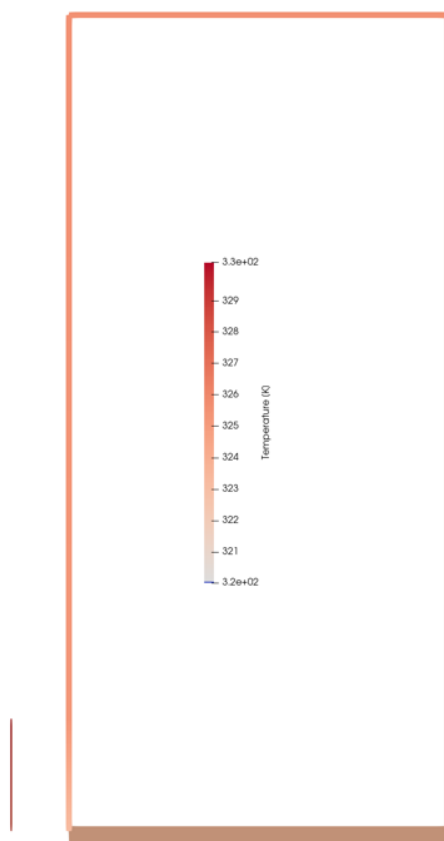Following the steady state calculation, a protected loss of forced convection (PLOFC) accident was simulated. Beginning at 1250 seconds, the power to both coolant pumps is lost, and the reactor core is scrammed. The reactor core is assumed to follow the ANS standard ANSI/ANS-5.1-2005 decay heat curve for U-235, while the coolant pumps are assumed to have a pump coast down time of 4.5 seconds. The heat transfer coefficient on the outer wall at the intermediate loop steam generator location is set to zero at 1250 seconds, forcing the system to reject the decay heat through the RCCS. The transient was simulated out to three days.

The core energy balance, core inlet and outlet temperature, and flow rate during the transient are shown in Figure 3-7, Figure 3-8, and Figure 3-9, respectively. Figure 3-10 shows the evolution of the flow rate early in the transient, when the transition from forced circulation to natural circulation is occurring. At the system level, the average channel model and the multi-channel model provide similar predictions. In both systems, the core flow rate decreases quickly, until a natural circulation flow rate of 13 kg/s is established. Figure 3-10 shows that the fluid diode opens shortly after the primary pump is tripped, about 30 seconds into the transient. After the fluid diode opens about half of the coolant flowing through the core enters the flow diode, the other half passes through the heat exchanger before returning to the downcomer. In the early stages of the transient, the thermal inertia of the intermediate system allows for cooling of the primary salt within the heat exchanger. As a result, a slight over cooling of the primary system occurs, leading to a decrease in the core inlet temperature. As the intermediate salt begins to heat up, the heat exchanger's contribution to heat rejection decreases, leading to an increase in the primary salt temperature. As the salt temperature increases, the reactor vessel wall temperature increases, and the heat rejected to the RCCS increases. This is evident in Figure 3-7 and Figure 3-12, which shows the temperature of the water within the RCCS.

While the average channel and multi-channel models show similar predictions at the system level, the multi-channel model offers a more granular look into the behavior of the reactor core. The maximum fuel temperature, shown in Figure 3-11, for the multi-channel model is higher than the average channel model. This result is expected due to the radial power profile that is specified in the multi-channel model. Additionally, the multi-channel model shows an increase in the outlet temperature in the early stages of the transient. This result can be explained by examining the flow rates and outlet temperatures of each channel, shown in Figure 3-13 and Figure 3-14. In the natural circulation regime, the buoyancy pressure head drives the flow within the channel. The higher power levels within the central channels causes a larger buoyancy pressure head leading to an increased flow rate within the central channels. In the early stages of natural circulation, before the pressure drops within the channels reach a new equilibrium, the outlet temperature of the central channel causes a greater increase in the outlet temperature of the core.

In general, the SAM predictions for the single channel and multi-channel models agree. Additional work is required to determine the feasibility of the RCCS and intermediate loop that were designed for this model. Future work will focus on making comparisons between the 1-D multi-channel model and the 2-D porous medium model, using the 1-D modeling improvements described in Section 2 of this report.
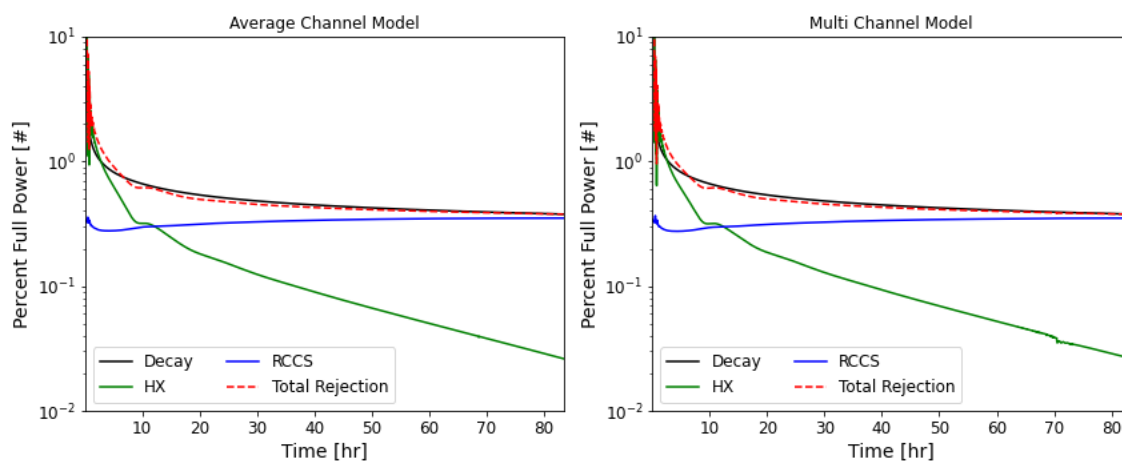
Figure 3-7. System energy balance for the average channel (left)
and multi-channel (right) model.
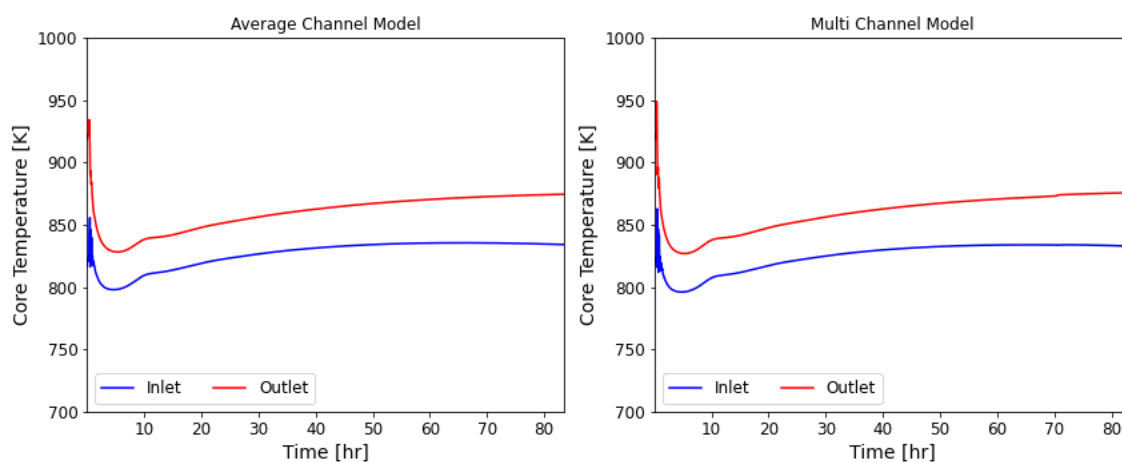
Figure 3-8. Core inlet and outlet temperature for the average channel (left)
and multi-channel (right) model.

Figure 3-9. Relative flow rate for the average channel (left) and multi-channel (right) model.

Figure 3-10. Relative flow rate in the early stages of the transient for the average channel (left) and multi-channel (right) models.

Figure 3-11. Maximum fuel temperature for the average channel (left) and multi-channel (right) model.

Figure 3-12. RCCS riser temperature for the average channel (left)
and multi-channel (right) model.

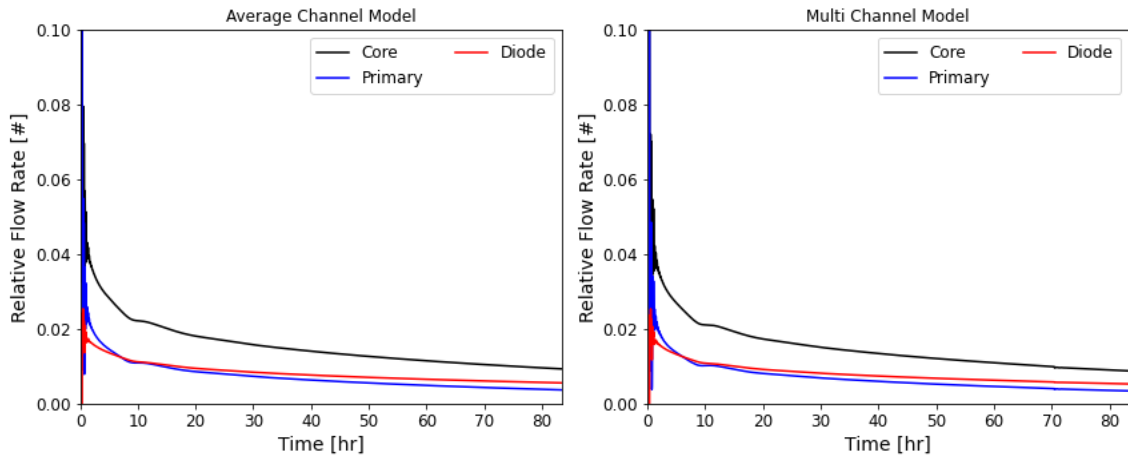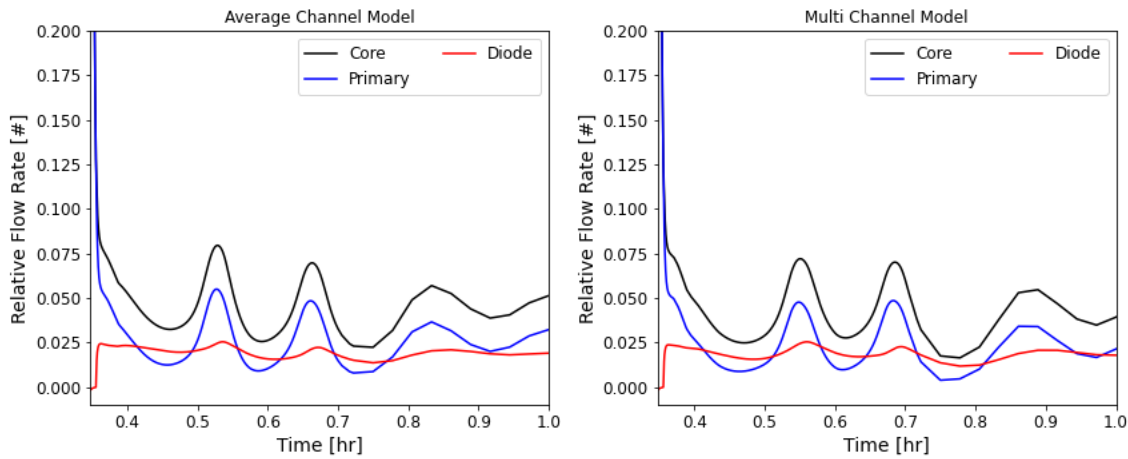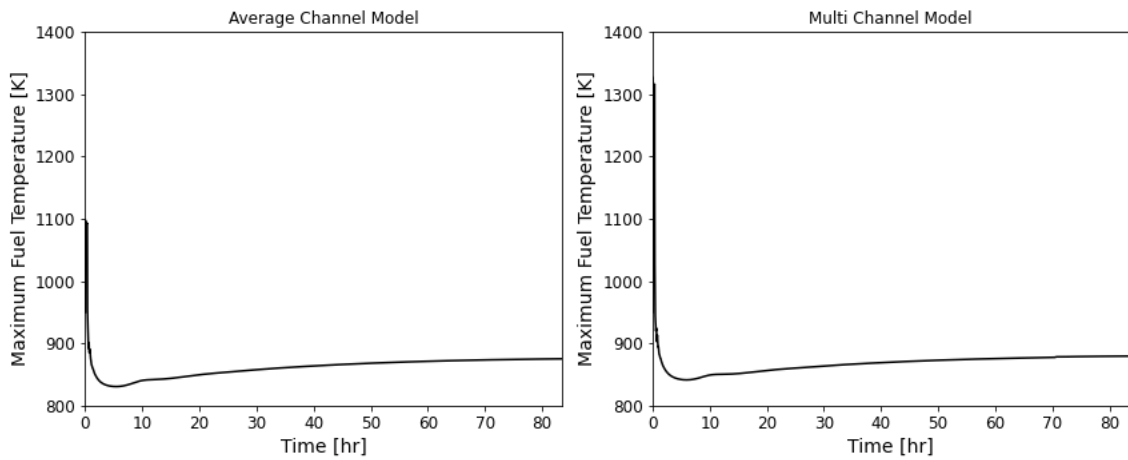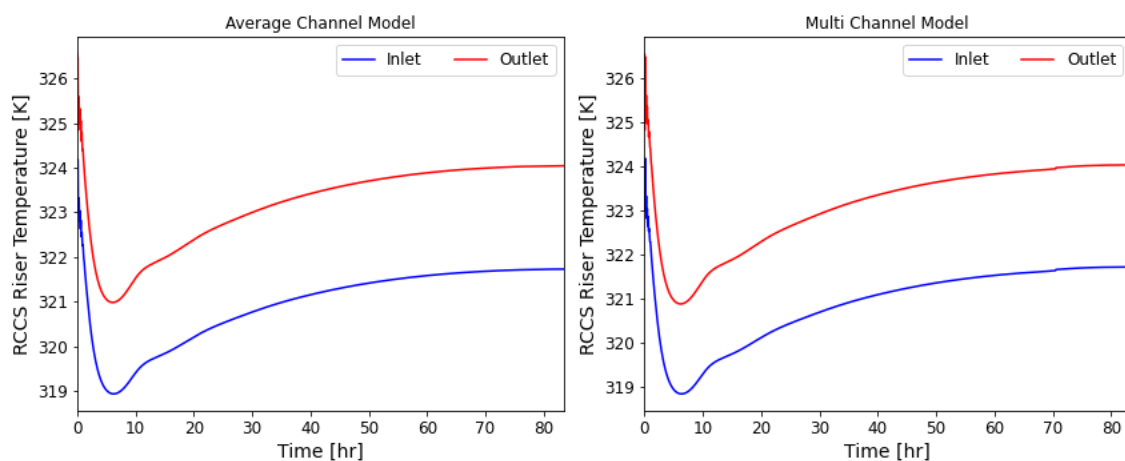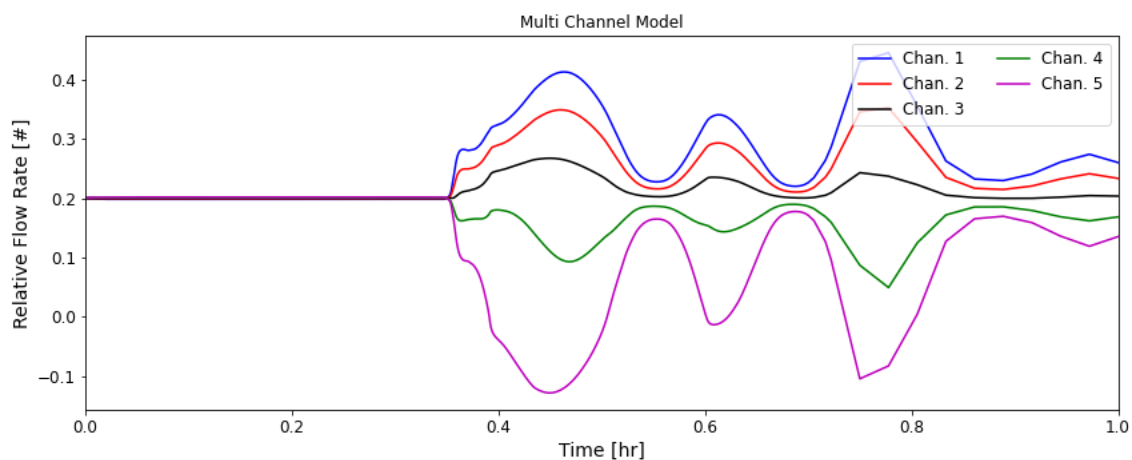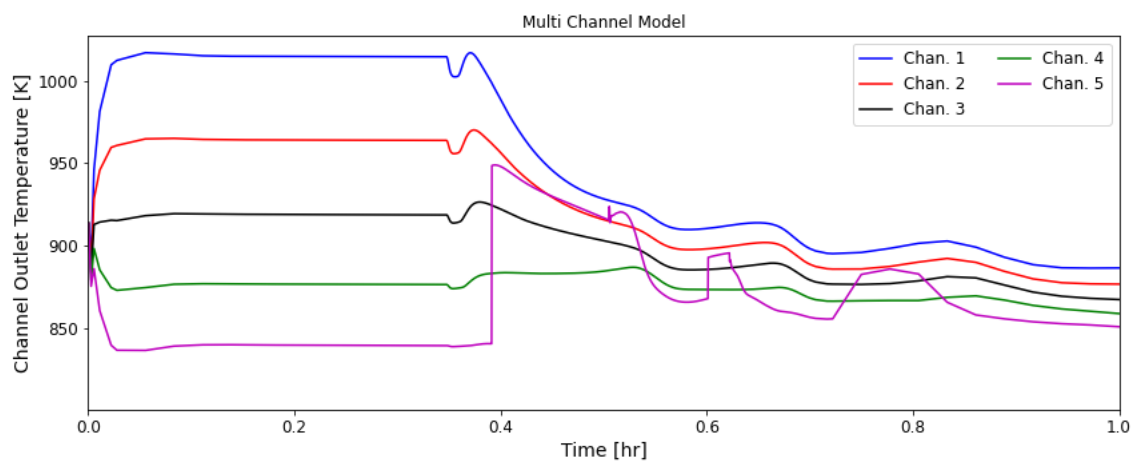Figure 3-13. Relative channel flow rate during the initial stage of the transient.

Figure 3-14. Channel outlet temperature during the initial stage of transients

4   Updates on CIET Benchmark Simulations

Previous work on the validation of the SAM against the Compact Integral Effects Test (CIET) experiments have been focused on the forced convection cooling transient tests, the steady-state DRACS (Direct reactor auxiliary cooling system)-DHX (DRACS heat exchanger) natural circulation tests, as well as the heater frequency response tests [22, 23].

In this study, we focused on the validation of SAM against the CIET Loss of Forced Circulation (LOFC) test. The PB-FHR LOFC is a postulated accident event which is initiated with the main coolant pump trips and reactor scrams, and subsequently, the reactor coolant flow transits from forced circulation to natural circulation to remove the decay heat via the DRACS. In the previous study, one of the main focuses was the steady-state DRACS/DHX natural circulation validation. In this study, the entire transient of LOFC is simulated, which includes the steady-state DRACS/DHX natural circulation as the final stage of the transient. The SAM modelling of the LOFC test takes advantages of the existing DRACS/DHX input model and the primary loop input model from the previous study. In this study, the two input models are integrated together to examine the transient evolution from normal operation in the primary loop to natural circulation heat removal in the DRACS/DHX loops upon the simulated loss of forced convection.

4.1 CIET LOFC Experimental Setup

The CIET experimental loop is a scaled-height, reduced-flow-area test facility designed, built and operated at the University of California, Berkeley [24, 25]. It aims to reproduce the thermal-hydraulic response of FHRs under forced- and natural-circulation conditions, and to provide experimental data to validate best-estimate computer codes in order to support their use in reactor safety and licensing analysis.

As shown in Figure 4-1, the CIET facility consists of two main flow loops, i.e., the primary loop and the DRACS loop. The primary loop essentially consists of an electrical heater (component '1' in Figure 4-1) that simulates the reactor core, a fan-driven air-cooled heat exchanger to simulate the coiled-tube air heater (CTAH), a pump to drive the coolant flow, as well as a primary loop shutoff valve (not shown) that can isolate the primary loop in an LOFC event. Additional to the heater branch, the primary loop also includes the DHX branch, as shown in Figure 4-1 (left). The CIET DHX branch of the primary loop simulates the prototypical DHX branch in the Mk1 PB-FHR design. The reactor design uses a fluid diode in the DHX branch to regulate the upward and downward flows. With high upward flow resistance, the device minimizes upward flow through the DHX and therefore parasitic heat loss to the DRACS loop for reactor normal operating conditions. Meanwhile, this limited upward flow keeps the DHX branch and DRACS warm to avoid potential salt freezing. For accident conditions, e.g., LOFC, because of low downward flow resistance, the fluid diode device does not affect the natural circulation flow in the heater-DHX subloop. In CIET, the fluid diode is simulated with a needle valve and a check valve in a parallel-flow arrangement.

The DRACS loop functions similarly to the DHX loop except that natural circulation is always present and the loop is constantly dissipating heat. The DRACS loop essentially consists of the DRACS side (tube side) of the DHX and a similar fan-driven air-cooled heat exchanger to simulate the thermosyphon-cooled heat exchanger (TCHX). It should be noted that both the CTAH and

TCHX analogue heat exchangers in the experimental setup are regulated by controlling their fan speeds and thus outlet temperatures.

For the CIET LOFC experiment, before the transient starts, the thermal-hydraulics conditions of the test facility were allowed to reach steady state for controlled pump coolant flow rate and heater power, to simulate the reactor normal operating condition. Under this condition, the primary loop flow rate was controlled at 0.18 kg/s, which includes the DHX bypass flow rate of 0.018 kg/s (obtained by manual adjustments to the needle valve), and the remaining 0.162 kg/s coolant flow through the heater section. The nominal heater power input is 6 kW, and CTAH and TCHX outlet temperatures of 80 °C and 46 °C, respectively.

From the normal operation mode, loss of forced convection was initiated by tripping the pump, reducing the nominal heater power input to 2 kW (representing the switch from fission heat production to decay heat) and isolating the primary loop by closing the shutoff valve. This event is schematically illustrated in Figure 4-1 (right). After pump trip, and consequently closing the shutoff valve, the coolant flow in the primary loop starts to decrease and then completely stops. Natural circulations in both the DHX-heater loop and the DRACS loops start to form, which transfers the heat from the DHX-heater loop to the DRACS loop, and eventually to the environment through TCHX. In CIET LOFC experiments, important data such as mass flow rates, power inputs as well as inlet and outlet temperatures of various components were collected throughout the experiment and were used for SAM validation in this study.
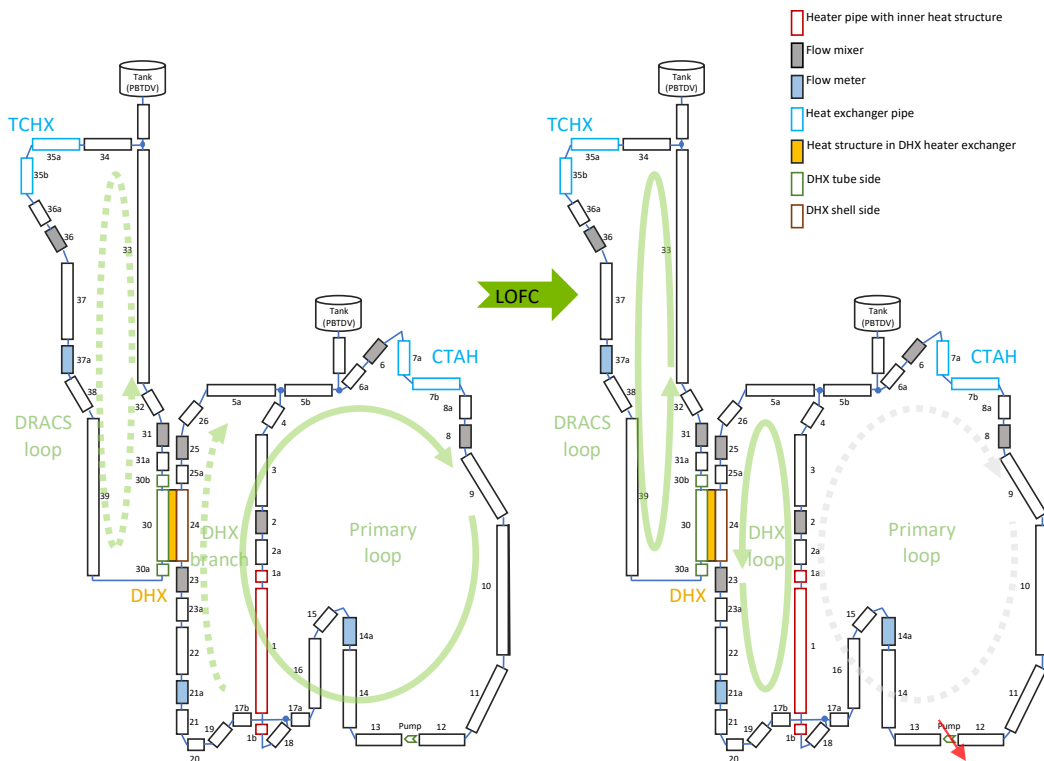

Figure 4-1. Diagram depicting the transition from (left) normal operation to (right) LOFC condition. The arrows show the flow direction while dashed lines imply reduced flow rate.

4.2 SAM Input Model

The SAM input model used in this study is largely based on the input models described in the previous validation study [22, 23], with the addition of a primary loop shutoff valve and several improvements to the temperature readout locations. The temperature readout locations referenced the CIET schematics to more accurately reflect the corresponding temperature sensors used in the CIET experimental setup. Compared with the experimental setup, some adjustments are made:

1) Effective heater power: The heater used in the experiment experienced a non-negligible parasitic heat loss to ambient, which meant that the effective heating power to the coolant was less than the supplied electrical power input. To correct this, we back-calculated the effective heater power from the heat balance at steady conditions, similar to the approach used in the previous validation study.

2) Pump trip and valve shutoff: To reproduce the effect of residual momentum in the experiment pump after tripping which resulted in a more gradual mass flow rate decline, we coasted down the pump in the SAM model with a linear decrease in pump head. Subsequently, we terminated the residual flow by closing the shutoff valve as it was performed in the experiment.

3) Check valve and needle valve arrangement: The check valve and needle valve arrangement in the experiment produced the necessary adjustable downward flow bias in the DHX. We reproduced the effect of the arrangement in the SAM model by imposing asymmetrical loss coefficients (K-loss coefficients), i.e., different upward and downward K-loss coefficient values, in the DHX loop. The upward flow loss coefficient was adjusted until the desired mass flow rate in the DHX loop was obtained under normal operating condition. This step was analogous to adjusting the needle valve in the LOFC experiment.

4) TCHX outlet temperature: The TCHX outlet temperature in the experiment was regulated by a controller that aimed to keep the outlet temperature at a constant 46 °C. However, due to the sudden increase in heat dissipation through the DRACS loop during LOFC, the TCHX outlet experienced a considerable temperature drift. Since the TCHX outlet temperature was an important boundary condition in the SAM model, we reproduced the time-dependent temperature by a set of polynomial function fittings of the actual TCHX outlet temperature sensor data, in order to better reflect the actual conditions in the experiment.

The important input parameters and times of the SAM model are summarized in Table 4-1 below.

Table 4-1. Summary of SAM input parameters and times used to reproduce the LOFC experiment.

Parameter	Experiment Time (s)	SAM Model Value
Heater Power (W) (Nominal)	2900 – 5952.1	5215.3 (6000)
	5952.1 – 5952.8	3818.8 (4393.4)
	5952.8 – 8100	1609.9 (2000)
Pump Head (Pa)	2900 – 5947.3	12411.2 [0.18 kg/s]
	5947.3 – 5956	12411.2 → 0
	5956 – 8100	0
Shutoff Valve	5963	Opened → Closed
CTAH Outlet Temperature (°C)	2900 – 8100	80
TCHX Outlet Temperature (°C)	2900 – 6075	46
	6075 – 8100	A set of polynomial functions (Appendix A)
Ambient Temperature (°C)	2900 – 8100	25

In the previous work [22, 23], to account for the parasitic heat loss observed in the CIET experiment, the heat transfer area densities of the CIET pipes and DHX was calibrated in the SAM model. The ratios of the calibrated values to that of the physical values at various parts of the experimental setup are tabulated in Table 4-2. It is clear that the calibration ratios are not uniform, and location dependent. As will be discussed later, this is most likely due to the nonuniform distribution of struts that fix pipes onto the test facility framework.

Table 4-2. Summary of heat transfer area densities and calibration ratios for components at various locations in the SAM model.

Location	Physical Value (m^{-1})	Calibrated Ratio
Global (except for locations specified below)	143.6	2.47
Top of DHX loop	143.6	10.5
Bottom of DHX loop	143.6	7.66
DHX external	78.7	25.4
DHX internal	629.9 (Tube side) 436.3 (Shell side)	1.80

These calibrated values were used in the initial LOFC SAM simulations. However, we observed that while the SAM results agree reasonably well with the experiment during the steady states before LOFC and towards the end of the experiment, the time response of the simulation during the LOFC transient was much slower than expected. This suggested that the thermal inertia in the SAM model was much larger than the actual values. Further investigation revealed that the large thermal inertia was caused by the artificially strong thermal coupling between the wall materials and the coolant due to the increased heat transfer area densities from the previous calibration procedure. Therefore, in the current calibration approach, we restored the heat transfer area densities to their original physical values, and instead calibrated the thermal conductivity of the pipe outer insulation (fiberglass) to match the parasitic heat loss to the ambient.

We have chosen to calibrate the thermal conductivity of the insulation (fiberglass) due to the following reasons:

1) The thermal conductivity of fiberglass insulation could exhibit high variability depending on the manner in which it was installed, such as the amount of insulation compression and whether air channels were present in the insulation.

2) Compounding to the point above, the nominal thermal conductivity of fiberglass is very close to zero. This meant that the ambient heat loss in the experiment would be very sensitive to the variation in fiberglass thermal conductivity.

3) Besides variations in fiberglass properties, the struts that were used to secure the CIET components to the structural frame attached directly to these components underneath the fiberglass insulation. This increased the 'effective thermal conductivity' of the outer fiberglass insulation from the perspective of the steel pipe walls.

In the current SAM model, we performed the calibration of the effective fiberglass thermal conductivity with respect to the experimental data towards the end of the LOFC experiment as it represented a steady state with low input power (i.e. higher temperature sensitivity to variations in ambient heat loss).

4.3 Validation Results

In the data analysis of the CIET LOFC experimental data (dated August 17, 2015), we found that one subset of the data (temperature data) contained a systematic time shift of approximately +25 seconds, leading to an apparent delay in temperature response during LOFC. The presence of the systematic error was confirmed by comparison with an earlier LOFC experiment (July 16, 2015) which did not exhibit this time shift. In light of this, the experimental data presented in this section has been corrected for this time discrepancy (-25 seconds).

In the SAM validation against the LOFC experiment, there are three important time periods of interest:

1) Pre-LOFC Steady State: The pre-LOFC steady state represents the normal operation mode and provides an opportunity to compare the simulation results under well-defined conditions (i.e. known mass flow rates, heater power, and temperature boundary conditions).

2) LOFC Transient: The LOFC transient refers to the short time period (~250s) after LOFC has been initiated. It provides an opportunity to evaluate the time response of the SAM model.

3) Post-LOFC Steady State: The post-LOFC steady state refers to the long time period after LOFC, where the transient behavior has sufficiently damped and approaches a new steady state driven by natural circulation.

The pre-LOFC steady state and LOFC transient are shown in Figure 4-2, which plots the SAM simulation and experimental results for the short time before and after LOFC. Meanwhile, the post-LOFC steady state is shown in the longer timescale plots in Figure 4-3. In the SAM model, the effective thermal conductivity of fiberglass had been calibrated to a factor of 4 times its physical value. In all plots of Figure 4-2 and Figure 4-3, the first and last dotted lines represent pump trip and shutoff valve closure, respectively, while the second dotted line represents zero pump head and lowering of heater power to 2 kW.
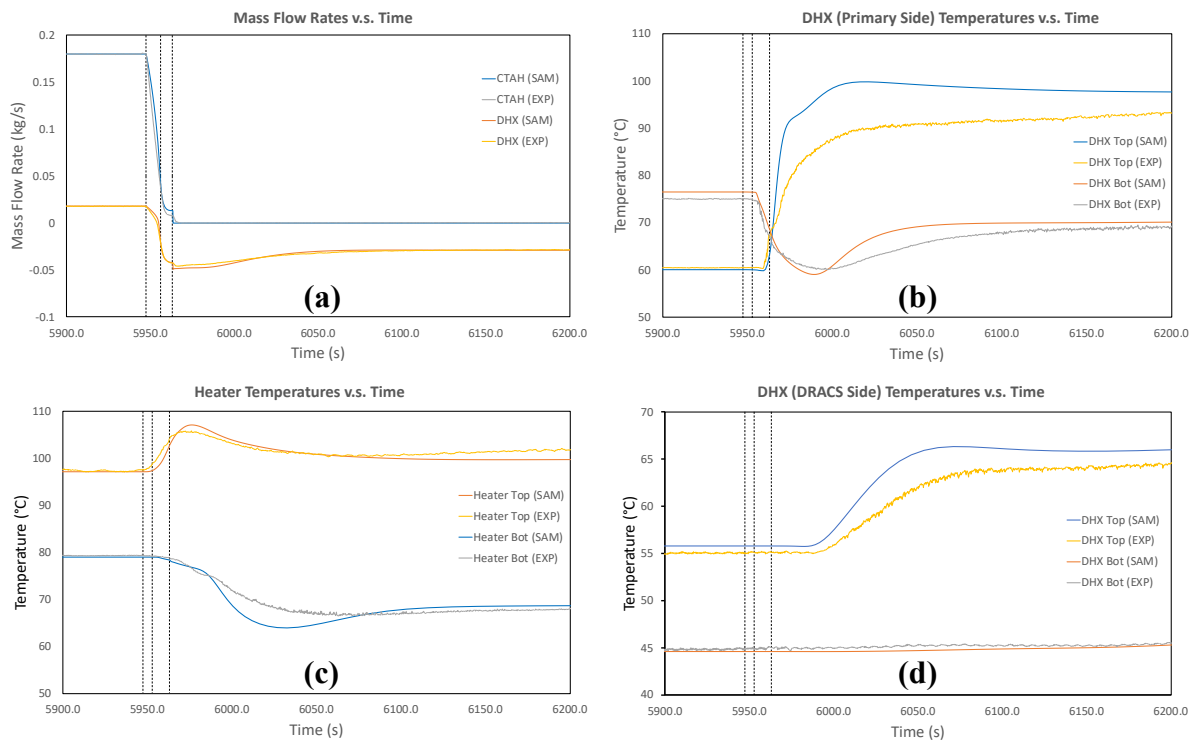
Figure 4-2. Mass flow rates and temperatures for the short timescale during LOFC.

In the mass flow rate graph in Figure 4-2 (a), the CTAH and DHX mass flow rates from the SAM simulation matched very well with the experiment in both the pre-LOFC steady state and the LOFC transient. However, the slight discrepancy in flow rates between zero pump head and shutoff valve closure suggests that the natural circulation driving force in the primary loop might be stronger in the SAM model and/or that some frictional losses were underestimated, such as from the stalled pump which was not modelled. There was also a slight discrepancy during the pump coast down period due to the lack of experimental parameters to describe the pump behavior

during this period. Nonetheless, the SAM simulation correctly predicted the flow reversal in the DHX loop with very good agreement. It is also noted that the DRACS natural circulation mass flow rate experimental measurement was not provided, and therefore not plotted here.

For the temperature results during pre-LOFC, the heater temperatures matched well with experiment data, as shown in Figure 4-2 (c). However, the DHX temperatures, both on the primary side (Figure 4-2 (b)) and DRACS side (Figure 4-2 (d)), showed a greater temperature change of approximately 2 °C as compared with experiment data. This could be due to an overestimation of the heat transfer in the DHX component of the SAM model. In the LOFC transient, the SAM model captured the expected temperature profiles during the transient. However, other than the heater temperatures which matched reasonably well, the larger magnitude of the temperature change and faster response in the DHX (both the primary and DRACS side) suggests that the thermal inertial in the SAM model could have been underestimated.
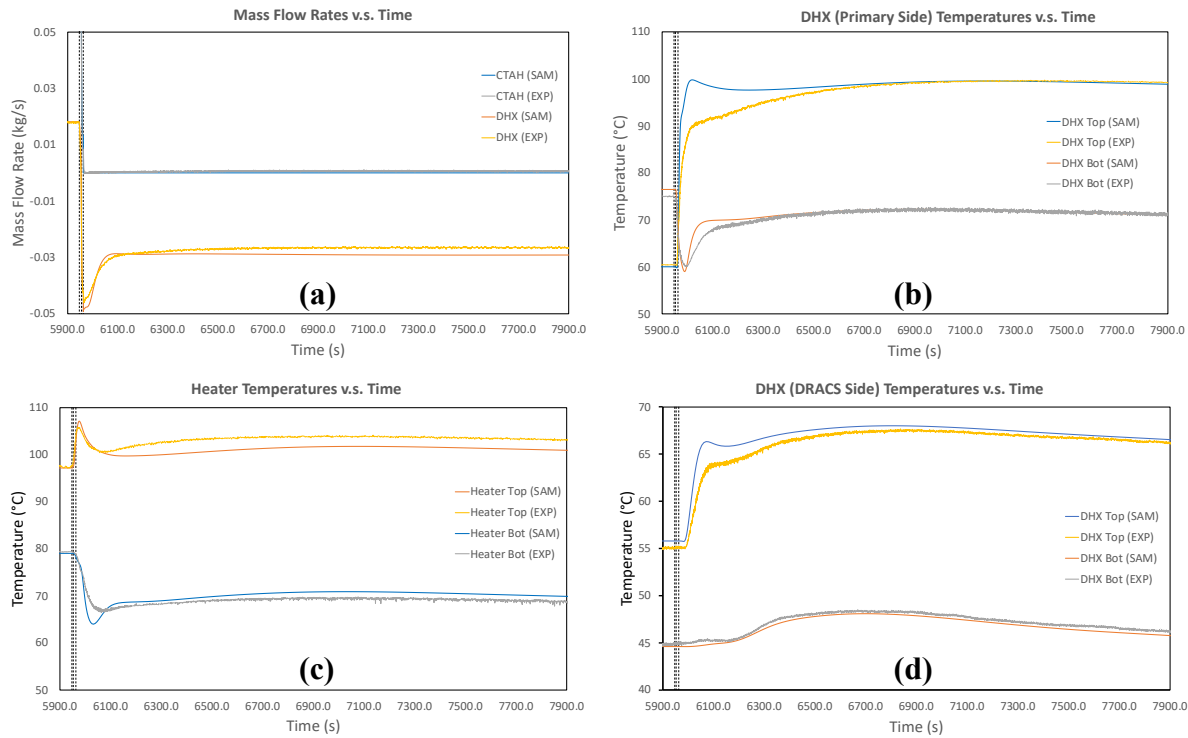

Figure 4-3. Mass flow rates and temperatures plotted against a longer timescale.

In the post-LOFC steady state, the mass flow rate in the SAM model appeared to be greater than that in the experiment. This was likely due to the partial closure of the check valve leading to a greater frictional loss in the experiment which was not included in the SAM model. As a result of the higher flow rate in the SAM model, the differences in inlet and outlet temperatures were smaller than in the experiment. Nonetheless, the discrepancies were small (less than 3 °C) and the temperature results matched very well with the experimental data. In a separate simulation, decreasing the mass flow rate in the SAM model to match the experimental value by imposing an

artificial loss coefficient[1] resulted in the correct values of temperature change and a better temperature match with the experiment.

4.4 Discussions and Future Work

4.4.1 Partial closure of check valve

In the SAM simulation, the mass flow rate results matched reasonably well with the experiment during the LOFC transient but was larger than the experiment during the post-LOFC period. This discrepancy in the post-LOFC period would require an extra loss coefficient to be added to the SAM model in order to match the experiment. However, while small discrepancies could be expected, the mismatch was unusual as the required increase in friction coefficient was too large to be adequately accounted for by the change in fluid velocity observed in the experiment.

We postulate that the higher form loss observed in the experiment post-LOFC was due to a partial closure of the check valve. During the initial pump coast-down, the change in flow in the DHX loop was largely driven by the inertia of the coolant fluid in the heater pipes as the slowing pump presented an increasing resistance to the flow in the primary loop. Because the change in flow path occurred in a short amount of time, the force on the check valve was able to push the valve seal fully open.

As the flow rate stabilized and the primary driving force switched from the changing fluid momentum to natural circulation forces, the force on the valve seal was weakened. Since the seal was held under a restoring tension, the weaker force allowed the seal to close partially, thereby increasing the effective form loss in the DHX loop during the post-LOFC period.

While we can reproduce the transient behavior of the check valve in the SAM model by adding a time dependent (or fluid velocity dependent) form loss function, we have chosen not to do so due to the lack of experimental data on the behavior of the check valve as well as to avoid overfitting the data in this validation work.

4.4.2 Non-uniform Parasitic Heat Loss

During the calibration step in the LOFC and DRACS-DHX simulations, we observed that the temperature drops between different pairs of sensor locations did not simultaneously match with the experiment for any given value of insulation thermal conductivity, even after imposing the correct mass flow rates. This implies that the heat loss through the struts played an important factor in influencing the total heat loss to the surrounding.

In the calibration approach in this work, we combined the variation in fiberglass thermal conductivity as well as the heat loss through the struts into a single 'global effective thermal conductivity scale factor' for the insulation. However, because the spacings of the struts were non-uniform in the experiment, the effective insulation thermal conductivity at different regions in the experimental setup would also be non-uniform. Therefore, while we had only calibrated one global scale factor to obtain a 'best fit' amongst the temperature drops, the reality of non-uniform effective thermal conductivity would require different sections of the experimental setup to have their own scale factors.

---

[1] An additional K loss of 100 was applied to a standard Schedule-10 pipe junction in the DHX loop.

The potential issues with the above would be that the SAM model could become overly calibrated, which runs counter to the goal of this validation work, and that there is a lack of experimental data to inform the appropriate scaling to be imposed. Nonetheless, since the approximate locations of the struts in the experiment are known, a potential extension would be to refine the SAM model by modelling the struts as coupled heat structures where heat loss can occur. This would not only allow us to improve the fidelity of the SAM model but also avoid over calibration of the SAM model.

4.4.3   Sensitivity analysis and uncertainty quantification

The SAM simulation results in this work were produced by modelling the CIET experiments based on one set of nominal conditions, i.e. the ambient temperature, TCHX and CTAH temperatures, measured mass flow rates, etc. In future work, it may be worthwhile to perturb these conditions in order to determine their transient and steady state effects on the SAM simulation. Other important variables that would benefit from such study include the effective insulation thermal conductivity scale factor, the component heat transfer area densities as well as the form loss coefficients. This would allow us to determine the sensitivity of the SAM model on the variations of these conditions as well as to quantify the uncertainty of the resulting mass flow rate and temperature results.

4.5 CIET Benchmark Summary

In this study, SAM validation has been successfully performed against CIET LOFC experiments. The SAM input model is largely based on input models from the previous validation study, and several improvements were made, such as the improved temperature readout locations and parasitic heat loss recalibration. In the previous study, the parasitic heat loss was modeled by increasing the heat transfer area densities of test facility pipes. During this validation study, it was found that the large nonphysical heat transfer coupling between the fluid and wall materials significantly affected the time characteristics (thermal inertia) of the fluid to transient changes in temperature and mass flow rates. To resolve this modeling issue, instead of directly adjusting the heat transfer area densities of pipes, the fidelity of the SAM input model was further improved by calibrating the effective thermal conductivity of the insulation layer and meanwhile restoring the physical heat transfer area densities of pipes. Using the improved SAM model and calibration approach, we were able to obtain good agreements between the SAM simulation results and the experimental data during the entire LOFC transient.

In future work, we believe that it would be worthwhile to further improve the SAM model fidelity by including the location-dependent struts into the model, as well as perform a sensitivity analysis and uncertainty quantification for both the transient and steady state conditions. It is also worthwhile to reperform validation for the forced convection cooling transient tests and the steady-state DRACS/DHX natural circulation tests, using the new parasitic heat loss model developed in this validation study.

5 Summary

The molten-salt-cooled pebble-bed reactor, or pebble-bed FHR (PB-FHR) is a promising candidate among advanced nuclear reactor concepts with its improved passive safety characteristics and high thermal efficiency. To support the development and utilization of the SAM code for PB-FHR safety analysis, activities on SAM code enhancements, reference plant model developments, and code validations were performed to support near-term industry and NRC needs. The 1-D spherical geometry heat conduction model was implemented in SAM and verified with several verification test cases. The porous medium pressure drop correlations for pebble bed were converted and implemented into the 1-D fluid flow model to support the modeling of 1-D system models with pebble beds. A reference primary loop model of PB-FHR was developed based on the UC Berkeley Mk1 FHR design and incorporated some open design features from Kairos Power's KP-FHR. A reference standard problem of the reactor primary loop model is foundational to the methodologies employed by NRC to verify the adequacy of computer codes and evaluation models. Additional SAM validation has been successfully performed against CIET LOFC experiments. Good agreements between the SAM simulation results and the experimental data were obtained during the entire LOFC transient.

While the SAM code has been significantly improved for FHR modeling and transient analysis, ongoing and future work is needed to enable its application in licensing analysis, including:

- Improvements to salt heat transfer models including closure models for convective heat transfer and thermal radiation effects.

- Improvements to 1-D salt freezing model for simulation of full flow blockage due to salt freezing.

- Continuous improvements to tritium transport model.

- Continuous code improvements to support mechanistic FHR source term evaluation.

- Additional code validations for FHR applications.

Acknowledgement

Reference:

[1]   R. Hu, "SAM Theory Manual," Argonne National Laboratory, ANL/NE-17/4, 2017.

[2]   R. Hu, L. Zou, and G. Hu, "SAM User's Guide," Argonne National Lab.(ANL), Argonne, IL (United States), 2019.

[3]   R. Hu, "Three-dimensional flow model development for thermal mixing and stratification modeling in reactor system transients analyses," *Nuclear Engineering and Design,* vol. 345, pp. 209-215, 2019.

[4]   R. Hu and Y. Yu, "A Computationally Efficient Method for Full-Core Conjugate Heat Transfer Modeling of Sodium Fast Reactors," *Nuclear Engineering and Design,* vol. 308, pp. 182-193, 2016.

[5]   L. Zou, G. Hu, and R. Hu, "Code Enhancement to SAM Multi-scale/multi-dimensional Heat Transfer Modeling Capabilities," presented at the 2020 American Nuclear Society Virtual Winter Meeting (Chicago, IL, US, 11/16/2020 - 11/19/2020).

[6]   C. J. Permann *et al.*, "MOOSE: Enabling massively parallel multiphysics simulation," *SoftwareX,* vol. 11, p. 100430, 2020.

[7]   K. Ahmed, R. Scarlat, and R. Hu, "Benchmark Simulation of Natural Circulation Cooling System with Salt Working Fluid Using SAM," in *NURETH-17*, Xi'an China, 2017.

[8]   H. Zhao, L. H. Fick, J. Herter, and B. Haugh, "Overview of Kairos Power Systems Code KP-SAM Development," presented at the NURETH-18, Portland OR, 2019.

[9]   R. Hu *et al.*, "SAM Co-Development to Support Fluoride-salt-cooled High-temperature Reactor Design and Licensing," Argonne National Lab.(ANL), Argonne, IL (United States), 2021.

[10]   L. Zou and R. Hu, "Recent SAM Code Improvement to Heat Transfer Modeling Capabilities," Argonne National Lab.(ANL), Argonne, IL (United States), 2019.

[11]   L. Zou and R. Hu, "SAM Code Validation on Frictional Pressure Drop through Pebble Beds," Argonne National Lab.(ANL), Argonne, IL (United States), 2020.

[12]   L. Zou, D. O'Grady, G. Hu, and R. Hu, "Explicit Modeling of Pebble Temperature in the Porous-medium Framework for Pebble-bed Reactors Applications," Argonne National Lab.(ANL), Argonne, IL (United States), 2021.

[13]   S. Ergun, "Fluid flow through packed columns," *Chem. Eng. Prog.,* vol. 48, pp. 89-94, 1952.

[14]   N. S. S. Commission, "Reactor core design of high-temperature gas-cooled reactors. Part 3: Loss of pressure through friction in pebble bed cores," Nuclear Safety Standards Commission, Berlin, Germany, 1981.

[15]   B. Eisfeld and K. Schnitzlein, "The influence of confining walls on the pressure drop in packed beds," *Chemical engineering science,* vol. 56, no. 14, pp. 4321-4329, 2001.

[16]   W. Reichelt, "Zur Berechnung des Druckverlustes einphasig durchströmter Kugel-und Zylinderschüttungen," *Chemie Ingenieur Technik,* vol. 44, no. 18, pp. 1068-1071, 1972.

[17]   C. Kang, "Pressure Drop in a Pebble Bed Reactor," Texas A & M University, 2011.

[18]   G. Hu, D. O'Grady, L. Zou, and R. Hu, "Development of a Reference Model for Molten-Salt-Cooled Pebble-Bed Reactor Using SAM," Argonne National Lab.(ANL), Argonne, IL (United States), 2020.

[19]   C. Andreades *et al.*, "Design Summary of the Mark-I Pebble-Bed, Fluoride Salt-Cooled, High-Temperature Reactor Commercial Power Plant," *Nuclear Technology,* vol. 195, pp. 223-238, 2016.

[20]   K. Power. "Generic FHR Core Model - Kairos Power." Kairos Power. kairospower.com/generic-fhr-core-model (accessed April 26, 2021).

[21]   S. E. N. V. W. T.-S. S. B. Line. "SQM's Concentrated Solar Power (CSP) Thermo-Solar Salts." SQM Europe N.V. Worldwide Thermo-Solar Salts Business Line. http://helioscsp.com/sqms-concentrated-solarpower-csp-thermo-solar-salts/ (accessed August 8, 2020).

[22]   L. Zou, R. Hu, and A. Charpentier, "SAM Code Validation using the Compact Integral Effects Test (CIET) Experimental Data," Argonne National Lab.(ANL), Argonne, IL (United States), 2019.

[23]   L. Zou, G. Hu, D. O'Grady, and R. Hu, "Code validation of SAM using natural-circulation experimental data from the compact integral effects test (CIET) facility," *Nuclear Engineering and Design,* vol. 377, p. 111144, 2021.

[24]   N. Zweibaum, "Experimental Validation of Passive Safety System Models: Application to Design and Optimization of Fluoride-Salt-Cooled, High-Temperature Reactors," UC Berkeley, 2015.

[25]   N. Zweibaum, Z. Guo, J. Kendrick, and P. Peterson, "Design of the Compact Integral Effects Test Facility and Validation of Best-Estimate Models for Fluoride Salt–Cooled High-Temperature Reactors," *Nuclear Technology,* vol. 196, no. 3, pp. 641-660, 2016.